

**Engineering-based Quantification of Cerebrospinal Fluid  
Dynamics and Central Nervous System Tissue Dynamic Motion  
Using Non-invasive Magnetic Resonance Imaging in Type I  
Chiari Malformation**

A Thesis

Presented in Partial Fulfillment of the Requirements for the

Degree of Master of Science

with a

Major in Biological Engineering

in the

College of Graduate Studies

University of Idaho

by

Gwendolyn L.M. Williams

Major Professor: Nathan Schiele, Ph.D.

Committee Members: Gabriel Potirniche, Ph.D.; Audrey Fu, Ph.D.; Russell Qualls, Ph.D.;


Bryn Martin, Ph.D.


Department Administrator: Ching-An Peng, Ph.D.

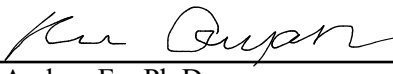
May 2021

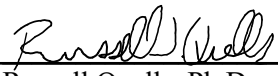
### Authorization to Submit Thesis

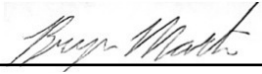
This thesis of Gwendolyn L.M. Williams, submitted for the degree of Master of Science with a Major in Biological Engineering and titled “Engineering-based Quantification of Cerebrospinal Fluid Dynamics and Central Nervous System Tissue Dynamic Motion Using Non-invasive Magnetic Resonance Imaging in Type I Chiari Malformation”, has been reviewed in final form. Permission, as indicated by the signatures and dates below, is now granted to submit final copies to the College of Graduate Studies for approval.


Major Professor:  Date: 4/12/2021  
Nathan Schiele, Ph.D.

Committee Members:  Date: 4/21/2021  
Gabriel Potirniche, Ph.D.

 Date: 4/12/2021  
Audrey Fu, Ph.D.

 Date: 4/12/2021  
Russell Qualls, Ph.D.

 Date: 4/12/2021  
Bryn Martin, Ph.D.

Department Administrator:  Date: 4/22/2021  
Ching-An Peng, Ph.D.

## Abstract

Chiari Type I Malformation (CMI) is a chronic central nervous system disease that is non-curatively treated with highly invasive brain surgery and has no standard metric to quantify successful surgery beyond symptom stabilization. The underlying CMI pathophysiology is not well understood, as the basis of this disease is physiologically tied to the flow of cerebrospinal fluid (CSF) but conflicting reports in literature have limited the use of CSF-based biomarkers for Chiari diagnosis and prognosis. The current standard for CMI diagnosis uses static morphometric measurements, which fail to relate to symptomology and therefore provide little basis for surgical outcome prediction and making appropriate surgical candidacy selection difficult. This research sought to address this issue of conflicting reports around CSF dynamics in CMI as well as work towards a better understanding of the underlying CMI pathophysiology.

Our objective here was to address the need for improved neuroimaging CMI diagnostic practices by investigating current imaging modalities and underlying pathophysiology with clinically relevant neuroimaging techniques and advanced post-processing methods. With a specific focus on using clinically relevant research, we applied engineering principles taken from cardiac engineering and apply them to the brain for diagnostics and prognostics of CMI. First, to address the need for improved CSF dynamics measurement techniques, we quantified agreement, reproducibility, and repeatability of 4D Flow and 2D PC MRI measurements of CSF velocities at the craniovertebral junction using a CMI subject specific in vitro model. Next, we utilized modern MR imaging and post-processing techniques to quantify differences in cardiac-induced neural tissue motion with novel parameters to represent relative displacement between physiologically relevant regions of interest.

We found an overall lack of reproducibility of PC MRI key measurements and dependent on the specific scanning machine used. With further research, machine-specific differences could be understood and potentially quantify these differences to develop a correctional calibration procedure. A standard calibration procedure could ensure results from any calibrated scanner are comparable to results from any other calibrated scanner. Our limited sample size showed preliminarily that neural tissue motion at the craniovertebral junction lacked statistically significant differences between patients and controls, neither before nor after posterior fossa decompression surgery. This finding is not supported nor rebuked by current literature regarding neural tissue motion in CMI, as reports are in great disagreement. There was some preliminary indication of a physiological relevance of relative neural tissue motion at craniovertebral junction. Relative neural tissue motion should be further studied with larger cohorts and imaging modalities with higher resolutions so that a biomarker could be defined that provides a better basis for surgical candidacy selection.

## **Acknowledgements**

In the process of writing this thesis, I have received a great deal of support and assistance.

I would first like to thank my supervisor, Dr. Bryn Martin, whose expertise was invaluable in the formulation and execution of the research presented here. Your dedication to improving the lives of the Chiari community has been truly inspiring to me.

I would like to acknowledge my other mentors and advisors, Dr. Audrey Fu, Dr. Gabriel Potirniche, and Dr. Nathan Schiele, for the dedication they've each shown me in completing this work. I would like to specifically thank Dr. Schiele for going above and beyond with his support at a critical and tenuous point. You provided me with the tools and assistance that I needed to complete this thesis successfully.

In addition, I would like to thank the kind and generous people of the American Syringomyelia & Chiari Alliance Project for providing the financial backing necessary to execute and complete the research presented here. It is truly humbling to be supported in this way, and I will continue to strive to produce deserving research.

### **Dedication**

The writing of this thesis has been long and difficult, and I could not have completed this work without the unending love and support of my husband and partner, Dylan Adams. You've been there for me since the start, always lending a sympathetic ear and open arms for me to land in. Truly and sincerely, thank you.

Finally, I would like to thank my family. To my parents, thank you for showing me the reward of hard work and the importance of love and laughter. To my sisters, Candy, and Maddy, thank you for being my best friends. Your love and support have always meant so much to me, now more than ever.

You've all made me who I am today, and for that, I cannot thank you enough.

## Table of Contents

Authorization to Submit Thesis.....	ii
Abstract.....	iii
Acknowledgements .....	iv
Dedication.....	v
Table of Contents .....	vi
List of Tables .....	viii
List of Figures.....	x
List of Equations.....	xiii
Statement of Contribution .....	xiv
Chapter 1: Introduction.....	1
Objective and Specific Aims .....	1
Chapter 2: Background.....	3
CMI Imaging Techniques.....	5
Mathematical Basis of Post Processing Techniques .....	6
Tables .....	8
Figures .....	9
Chapter 3: In Vitro Evaluation of Cerebrospinal Fluid Velocity Measurement in Type I Chiari Malformation: Repeatability, Reproducibility, and Agreement using 2D Phase Contrast and 4D Flow MRI.....	13
Abstract.....	13
Introduction .....	15
Literature Review .....	16
Methods .....	18
Results .....	21
Discussion.....	23
Limitations.....	26

Conclusion .....	27
Tables .....	28
Figures .....	35
Chapter 4: Quantification of Cardiac-Related Neural Tissue Motion in Type 1 Chiari Malformation: A Case Control Study pre- and post-Spinal Decompression Surgery .....	41
Abstract.....	41
Introduction .....	42
Methods and Materials .....	43
Results .....	47
Discussion.....	48
Tables .....	52
Figures .....	57
Chapter 5: Conclusion .....	65
Future Directions .....	66
References .....	68
Appendix A .....	75
Tables .....	75
Figures .....	76
Appendix B.....	77
Tables .....	77
Figures .....	78
Appendix C: Institutional Review Board Approval Letter.....	81

## List of Tables

<b>Table 2.1.</b> Symptoms of CMI [3].....	8
<b>Table 3.1.</b> Literature review of 2D PC MRI (N = 208) and 4D PC MRI (N = 49) in vivo measurements of peak CSF velocities in healthy (H, N = 91) and Chiari malformation patient (P, N = 166) cases (Note: the peak velocities denoted by an asterisk were measured at points/probes and not throughout the axial plane). H* indicates healthy subjects with a syrinx. ....	28
<b>Table 3.2.</b> Literature review of repeatability, reproducibility, and agreement studies of PC MRI fluid velocity quantification techniques. ....	30
<b>Table 3.3.</b> MRI protocols used for 2D PC MRI and 4D Flow MRI acquisition.....	31
<b>Table 3.4.</b> Distance of between axial planes imaged. ....	32
<b>Table 3.5.</b> Effect sizes and corresponding p values estimated from the linear mixed-effects model for velocity measurements. The mean effect size is provided, along with the 95% confidence interval (CI). We used Bonferroni correction to account for multiple testing. * represents statistical significance under Bonferroni correction where $p < 0.05/14=0.0036$ . ....	33
<b>Table 3.6.</b> Standard deviations of scanning centers for scanning type data subsets and over the entire dataset. ....	34
<b>Table 4.1.</b> Literature review of previous studies detailing tissue motion at the craniovertebral junction. * represents studies that found a statistically significant difference between untreated Chiari malformation type I (CMI) patients and healthy controls. ....	52
<b>Table 4.2.</b> Clinically reported symptoms for all patients before surgical intervention. ....	53
<b>Table 4.3.</b> Results of statistical analysis using linear mixed effects model (LME) before and after false discovery rate adjustment (FDR). * represents statistically significant values after adjustment at the 0.10 level. ....	54
<b>Table 4.4.</b> Results of all statistical comparisons across groups, before and after adjustment. * represent statistically significant results to the 0.1 level. ....	55
<b>Table 4.5.</b> Summary of results and descriptive stats for all pre- and post-operative patients and controls. ....	56
<b>Table A.1.</b> Effect sizes and corresponding p values estimated from the secondary linear mixed-effects model for velocity measurements. This model uses Center 2 as the baseline and includes interactions between scanning modality, scanning center, and axial position of imaging. The mean effect size is provided, along with the 95% confidence interval (CI). We used Bonferroni correction to account for multiple testing. * represents statistical significance under Bonferroni correction where the threshold is $p < 0.05/14=0.0036$ . ....	75



<b>Table B.1.</b> Pearson correlation coefficients (CC) for peak spinal cord impaction and tonsillar position for each group.....	77
---	----

### List of Figures

**Figure 2.1.** In the normal brain, the tonsils stay above the foramen magnum. In Chiari malformation type I, the tonsils descend into the upper cervical canal (the top of the neck) [7]. ..... 9

**Figure 2.2. a)** Exemplary portion of a theoretical pulse sequence diagram for a spin echo MRI with 90° radio frequency pulses (RF) and some positive gradient that could represent such things as slice-select, frequency encoding, displacement encoding, etc. **b)** Corresponding orientation of protons before and after application of magnetic gradient (RF pulses here) based on the timing indicated in the pulse sequence diagram in **(a)**. ..... 10

**Figure 2.3.** Example phase contrast magnetic resonance image (PC MRI) of Chiari patient at a mid-point in the cardiac cycle. .... 11

**Figure 2.4.** Graph depicting linear transformation of PC MRI image into velocity data. .... 12

**Figure 3.1.** Summary of the average peak CSF velocities reported in 2D PC MRI **(a)** and 4D PC MRI **(b)** literature for healthy subjects and Chiari malformation patients pre-decompression surgery. Average values in figure are weighted by number of subjects within each study. Error bars represent pooled reported standard deviation for studies included in each group. The total number of healthy and Chiari malformation patient studies included is 91 and 166, respectively (see **Table 3.1** for individual values). FM = foramen magnum. .... 35

**Figure 3.2. (a)** Development of in vitro models based on subject specific scans. First, subjects were scanned to produce a T2 anatomical MRI and a 4D Flow MRI. The anatomical MRI was then used as a basis for the 3D model. The 4D Flow MRI allows the determination of the cerebrospinal fluid (CSF) flow waveform which informs a computer-controlled pump. The model is then connected to the pump and scanned at each MRI center. **(b)** Cross section of the completed model. .... 36

**Figure 3.3.** Axial positions of 2D PC MRI and 4D Flow MRI velocity measurements with flow inlets and outlets indicated. Distance between imaging planes can be found in **Table 3.4**. A = anterior, P = posterior, S = superior, I = inferior; FM = foramen magnum. .... 37

**Figure 3.4.** Bland-Altman plot showing agreement between 2D PC MRI and 4D Flow measurements; the trendline of the data is indicated by the black line, the mean of the differences is shown in blue, and the mean ± 2STD is indicated by the red lines. .... 38

**Figure 3.5.** Box plot showing the difference between average velocity measurement at each axial location and each individual axial velocity measurements at each center. Top and bottom of boxes indicate 25<sup>th</sup> and 75<sup>th</sup> percentile of values with horizontal lines indicating the median of each value set and outliers represented as red cross marks. .... 39

<b>Figure 3.6. (a)</b> Peak systolic 2D PC MRI CSF velocity at each axial position for each center. <b>(b)</b> Peak systolic 4D Flow CSF velocity at each axial position for each center. Error bars shown represent standard deviation.....	40
<b>Figure 4.1.</b> Representative subject p04C scan with regions of interest (ROIs) drawn in: (1) Pons, (2) Cerebellar tonsil, (3) Upper Spinal cord and lower medulla.....	57
<b>Figure 4.2.</b> Displacement and impaction time-series data for representative subject p04C. Solid lines indicate displacement results for specific regions of interest (ROIs), while dotted lines indicate the difference, or impaction, of two ROIs. The points indicated by (a) and (b) represent peak absolute displacement. ....	58
<b>Figure 4.3.</b> Peak absolute displacements for all pre- and post-operative patients and controls of each region of interest (ROI). Horizontal bars represent the median value for a dataset, with the upper and lower limits of each box representing the 75 <sup>th</sup> and 25 <sup>th</sup> quartiles, respectively. Red cross marks represent outliers. ....	59
<b>Figure 4.4.</b> Peak absolute impaction results for all pre- and post-operative patients and controls of each region of interest (ROI). Horizontal bars represent the median value for a dataset, with the upper and lower limits of each box representing the 75 <sup>th</sup> and 25 <sup>th</sup> quartiles, respectively. Red cross marks represent outliers. ....	60
<b>Figure 4.5.a.</b> Regression analysis plots for all pre- and post-operative patients and controls showing tonsillar position versus tissue motion for peak impaction of the spinal cord – tons. <b>b.</b> Regression analysis plots for all pre- and post-operative patients and controls showing tonsillar position versus tissue motion for peak impaction of the spinal cord – pons.....	61
<b>Figure 4.6.</b> Bland-Altman of displacement results for each operator.....	62
<b>Figure 4.7.</b> Forest plot of meta-analysis showing previous studies which reported comparable metrics of tissue motion in the cerebellar tonsils or upper spinal cord. * represents studies that found a significant difference between pre-operative patients and controls. ....	63
<b>Figure 4.8.a.</b> Spinal Cord – tonsil impaction data shown over the cardiac cycle for all pre-operative patients and controls. <b>b.</b> Spinal Cord – pons impaction data shown over the cardiac cycle for all pre-operative patients and controls. ....	64
<b>Figure A.1.</b> Forest Plot of meta-analysis separated by imaging modality (2D PC MRI and 4D PC MRI) and Chiari vs healthy populations. <b>(a)</b> 2D PC MRI reported results for Chiari subjects. <b>(b)</b> 2D PC MRI reported results for healthy volunteers. <b>(c)</b> 4D PC MRI reported results for Chiari subjects. <b>(b)</b> 4D PC MRI reported results for healthy volunteers. ....	76
<b>Figure B.1.</b> Velocity timeseries data for representative subject p04 before and after applying net-zero velocity constraint. ....	78

**Figure B.2.** Regression analysis of operators 1 and 2 with linear trendlines shown for each region and R2 reported with color coding for respective regions of interest (ROIs): upper SC = spinal cord, pons, and tonsil. Black line represents linear trendline for all data points, with R<sup>2</sup> shaded with grey. .... 79

**Figure B.3.** Regression analysis plots for tonsillar position (TP) measurements vs each region of interest (ROI) investigated here (spinal cord = SC, tonsil, pons) for all patients and controls. Green dotted lines represent linear trendline of the data with R<sup>2</sup> reported. **(a)** Peak absolute spinal cord motion versus tonsillar position. **(b)** Peak absolute cerebellar tonsil motion versus tonsillar position. **(c)** Peak absolute pons motion versus tonsillar position. .... 80

**List of Equations**

Equation 2.1.....	6
Equation 2.2.....	6
Equation 2.3.....	6
Equation 2.4.....	7
Equation 2.5.....	7
Equation 2.6.....	7
Equation 3.1.....	20
Equation 3.2.....	20
Equation 3.3.....	21
Equation 4.1.....	46
Equation 4.2.....	46

## Statement of Contribution

Bryn Martin and Mark Luciano conceived of the ideas presented here and secured research funding for the work. Gwendolyn Williams led publications of manuscripts and overall presentation of results. Gwendolyn Williams, Bryn Martin, and Mark Luciano developed the theory. Imaging and data used in Chapter 3 was collected and analyzed by Suraj Thyagaraj with assistance from Bryn Martin. Imaging and data used in Chapter 4 was collected by Bryn Martin, John Oshinski, Mark Luciano, and John Tew. Analysis of data presented in Chapter 4 was analyzed by Gwendolyn Williams. The parameters for these studies were developed by Bryn Martin with some assistance from Gwendolyn Williams. Audrey Fu provided guidance for all statistical analysis here and drafted both Statistics sub-sections in the Materials and Methods presented in Chapters 3 and 4. Gwendolyn Williams drafted the manuscript and figures. All authors provided critical feedback and commented on the manuscript.

Authors:

Gwendolyn Williams: Department of Chemical and Biological Engineering

University of Idaho, Moscow, Idaho

Bryn Martin: Department of Chemical and Biological Engineering

University of Idaho, Moscow, Idaho

Alcyone Therapeutics, Inc.

Lowell, MA

Nathan Schiele: Department of Chemical and Biological Engineering

University of Idaho, Moscow, Idaho

Audrey Fu: Department of Mathematics and Statistical Science

University of Idaho, Moscow, Idaho

Mark Luciano: Department of Neurosurgery

Johns Hopkins University, Baltimore, Maryland

Suraj Thyagaraj: Department of Mechanical Engineering, Conquer Chiari Research Center

University of Akron, Akron, Ohio

John Oshinski: Department of Radiology and Imaging Sciences

Emory University, Atlanta, Georgia

John Tew: Department of Neurosurgery

University of Cincinnati Neuroscience Institute, Cincinnati, Ohio, and

University of Cincinnati College of Medicine, Cincinnati, Ohio, and

Mayfield Clinic, Cincinnati, Ohio

Daniel Giese: Department of Radiology

University Hospital of Cologne, Cologne, Germany

Alexander C. Bunck: Department of Radiology

University Hospital of Cologne, Cologne, Germany

Eleonora Fornari: Center for Biomedical Imaging, Department of Radiology

Centre Hospitalier Universitaire Vaudois, Lausanne, Switzerland, and

University of Lausanne, Lausanne, Switzerland

Francesco Santini: Division of Radiological Physics, Department of Radiology

University Hospital of Basel, Basel, Switzerland, and

Department of Biomedical Engineering

University of Basel, Allschwil, Switzerland

Francis Loth: Department of Mechanical Engineering, Conquer Chiari Research Center

University of Akron, Akron, Ohio



## Chapter 1: Introduction

Type I Chiari Malformation (CMI) is a poorly understood quality of life disease whose diagnosis and intervention techniques do not consistently result in effective treatment. At present, the diagnostic practice for CMI is based on a static measurement of cerebellar tonsillar ectopia and can be radiographically diagnosed in 1 in 1,000 individuals but, of those radiographically diagnosed, only some 14% have symptomatic CMI, while others are considered to be asymptomatic [1, 2]. That is to say, some of those radiographically diagnosed with CMI would have never known had it not shown up incidentally when their brain was imaged for other, often unrelated, issues. Of those with symptoms, not all will need to receive the standard treatment of a bony decompression surgery and only some who do receive surgical intervention will report an alleviation of their symptoms. The current standard diagnostic practice for CMI does not provide an accurate basis for prediction of surgical outcomes, nor does it identify true, symptomatic and clinically relevant cases of CMI.

Improved neuroimaging techniques are required to define a novel CMI biomarker that provides an accurate basis for prediction of surgical outcomes. CMI is a dynamic disease affecting the movement of cerebrospinal fluid (CSF), yet diagnostic practice is to utilize a static 2D image of the brain. Dynamic neuroimaging techniques with a dynamic biomarker must be applied to properly characterize the underlying CMI physiology. Advanced dynamic imaging techniques require longer scan times and are therefore too costly for clinical application at present.

To improve CMI diagnostic practices, we sought to investigate current imaging modalities and the underlying CMI pathophysiology with advanced neuroimaging techniques. To better understand current CSF measurement techniques, we evaluated the agreement, repeatability, and reproducibility of CSF quantification techniques used clinically and in research. We also utilized modern magnetic resonance (MR) imaging and post-processing techniques to quantify differences in cardiac-induced neural tissue motion to further characterize the underlying CMI pathophysiology.

### Objective and Specific Aims

#### *Objective*

Address need for improved neuroimaging CMI diagnostic practices by investigating current imaging modalities and underlying pathophysiology with clinically relevant neuroimaging techniques and advanced post-processing methods.

*Specific Aim 1*

Address need for improved CSF dynamics measurement techniques by quantifying agreement, reproducibility, and repeatability of 4D Flow and 2D PC MRI measurements of CSF velocities at the craniovertebral junction.

*Specific Aim 2*

Utilize modern MR imaging and post-processing techniques to quantify differences in cardiac-induced neural tissue motion with novel parameters to represent relative displacement between physiologically relevant regions of interest.

## Chapter 2: Background

Type I Chiari malformation (CMI) is an understudied quality of life disorder of the central nervous system traditionally characterized by cerebellar tonsillar descent greater than 5 mm below the foramen magnum resulting in a range of symptoms from mild neck pain to clinical depression with headaches as the hallmark sign. Clinical presentation of CMI can vary between pediatric and adult patient populations [3] as well as having higher prevalence in adult women than adult men in the United States [1, 4, 5]. McClugage et al [3] found CMI symptoms can be stratified based on their relation to 1) CSF obstruction, 2) symptoms related to brainstem or cerebellar compression, and 3) symptoms related to spinal cord dysfunction/syringomyelia (**Table 2.1**, [3]). Headaches caused by Valsalva activities are the most common symptom associated with up to 40% of symptomatic CMI cases; which is to say that potentially painful headaches affect up to 40% of this patient population as frequently as when they cough, laugh or sneeze [6].

The current understanding of CMI stratifies the causes of this malformation into two groups: primary or congenital Chiari malformation (CM) wherein the malformation is caused by structural defects incurred during fetal development for a variety of reasons, and secondary or acquired CM, which occurs later in life due to traumatic injury, disease, or infection. The exact pathophysiology of secondary CM is not known at present, but the presentation of primary and secondary CM is not known to differ. In the CMI disease state, the malformation refers to cerebellar tonsillar ectopia, when the lower portion of the cerebellum extends below the foramen magnum forming cerebellar tonsils, one on each left and right side, depicted below by Humphrey [7] (**Figure 2.1**). In a healthy state, only the spinal cord occupies this space, allowing the free movement of cerebrospinal fluid (CSF) through the spinal canal and ventricular system. At present, the only treatment available for CMI is posterior fossa decompression, which focuses on easing symptoms or impeding progression of damage to the central nervous system (CNS). This surgical intervention can be as minor as a removal of a small portion of the bone at the base of the skull, a craniectomy, or as serious as removal of the cerebellar tonsils entirely using electrocautery, or thermal cauterization of the tissue. CMI symptoms cover a wide range, with little consistency beyond headaches after coughing or sneezing, making it difficult to identify separately from associated CSF disorders such as hydrocephalus, spina bifida, and syringomyelia. In CMI patients, the ‘sinking’ of the cerebellum, or tonsil herniation, below the foramen magnum crowds the spinal cord and blocks the flow of CSF. CSF flow blockages can result in impaired function of the cerebellum, pons, medulla, and surrounding regions of the craniovertebral

junction. Further, CSF is central the brains circulation and waste clearance, which could be fundamentally impaired by the blockage caused in the CMI disease state.

CMI is radiologically diagnosed based on the extent of the cerebellar tonsillar ectopia, where either or both cerebellar tonsils must extent more than 3-5 mm below the foramen magnum but can be further classified by the presence of symptoms, symptomatic CMI, or the lack thereof, asymptomatic CMI. Oftentimes, CMI is found incidentally when someone receives a brain scan for unrelated issues and a Chiari malformation is noticed, making exact estimations of occurrence difficult and limiting research. At present, the significance of asymptomatic CMI is not understood. CMI research studies often do not include asymptomatic cases of CMI as they do not need surgical intervention and can be difficult to enroll in studies due to their limited presence in clinics. It is estimated that CMI prevalence is in the range of 1 in 1,000 to 1 in 5,000 individuals [1], but these could include incidental findings of asymptomatic CMI, which could be 0.9-14% of these cases [2, 8-10]. In a study by Vernooij et al [9], 2000 MRI scans of the general population were analyzed for incidental brain findings and 0.9% of scans has tonsillar ectopia extending more than 5 mm below the foramen magnum, with a mean herniation of 6.4 mm, ranging from 5.2 to 10.3 mm. Meadows et al. [2] reviewed 22,591 head and cervical spine scans of the general population and diagnosed 175 cases CMI with tonsillar descent 5 mm or greater wherein 25 of these (14%) were asymptomatic. Further, O'Reilly et al. [10] analyzed 147 volunteers without CMI symptoms, hydrocephalous, or space occupying lesions and found 2 radiological diagnosis of CMI as well as showed no significant correlation between tonsillar descent and symptomatology. These studies show that the current diagnostic practices do not accurately capture symptomatic cases of CMI and may be of limited diagnostic and prognostic utility.

The accepted standard diagnostics for CMI seem to fail to represent symptomatology and provide little to no basis for long term outcomes, thereby making selection of surgical candidates difficult and subjective to the clinic from which the diagnosis came. This may be due to the static nature of current diagnostic techniques, wherein a single mid-sagittal image is taken of the brain at any point in the cardiac cycle and used to measure tonsillar descent. The underlying CMI pathophysiology is dynamic in nature as it relates to the blockage of CSF flow over the cardiac cycle, inducing neural tissue motion that cannot be accurately captured with a single image at a random time point across the cardiac cycle. This fundamental mismatch in the underlying CMI pathophysiology and current diagnostic practice results in a surgical solution that only affects symptoms, not the underlying cause.

## CMI Imaging Techniques

Magnetic resonance imaging (MRI) is a common imaging modality used to take either static or dynamic images of the brain with specific properties allowing the differential viewing of bones, fatty tissue, and/or fluids for various clinical and research purposes. The basic principle of an MRI scan is as follows: biological tissue is comprised of hydrogen protons which contain nuclei that possess a “spin” property [11]. This spin property is essentially what allows this imaging to occur, as protons that can “spin” are excitable, which is to say that can be transitioned from low-energy states to high-energy states with applied magnetic fields (**Figure 2.2**). The timing of the applied magnetic fields, or magnetic gradient, is determined by a pulse sequence, depicted by pulse sequence diagrams. A portion of a simple, theoretical pulse sequence diagram is shown in **Figure 2.2.a**, wherein the timing of radio frequency (FR) and gradient pulses is shown with the corresponding change in proton orientation at each time point (**Figure 2.2.b**). As these protons transition back from their high-energy states to their low-energy states, they emit a small voltage that can be detected, amplified, and recorded. The time it takes for this proton to return to normal is directly related to the induced voltage, allowing a period of brief excitation and relaxation cycles to form an image of the proton’s characteristic frequency. The resulting image can therefore delineate tissue types based on pixel intensity, as different tissue types will have different characteristic frequencies. This basic concept can be expanded on, and specialized encoding gradients can be used to encode protons for kinetic values such as velocity or displacement, allowing more advanced analysis of tissue and fluid dynamics.

In clinical settings, standard practice is to use mid-sagittal 2D magnetic resonance (MR) images, x-ray imaging, or computed tomography (CT) to obtain a head and cervical spine scan for the purpose of measuring tonsillar ectopia and radiologically diagnosing CMI. These scans are fairly short, using a basic protocol dependent on preferences and standard practices of the clinic in which it occurs. Longer and more focused CSF flow studies can be requested by the attending neurologist to better assess surgical candidacy, but the use of these sequences are never for diagnostic purposes as currently no CSF-based biomarkers exist in CMI. These longer flow studies can use more advanced imaging techniques such as cine sequences to capture dynamic videos and pixel tagging encoded for velocity in multiple directions. Videos of CSF flow can show clinicians the actual movement and blockages of CSF flows, identifying structures with impeded flow or excessive motion, as well as CSF leaks and directional changes in flow pre- versus post-operatively. The most widely used method for CMI flow studies is 2D PC MRI (**Figure 2.3**), which is advantageous in its short scan time and ease of analysis for morphological and functional alterations, allowing for both qualitative and quantitative CSF characterization but is limited in its single-plane imaging and through plane

encoding restricting the ability to look in detail at complex flow patterns that occur in the CMI disease state.

More recently, novel PC MRI methods such as 4D Flow and DENSE imaging allow for three-dimensional encoding, resulting in more robust CSF flow analysis as well as the ability to produce computational flow dynamics (CFD) simulations based on these. As with any technique, these advanced modalities are difficult to implement in clinical settings as they have long scan times that are hard to schedule and expensive for patients, and the relevance of CSF dynamics as a metric for CMI remains under debate by the medical community. This lack of adoption of CSF dynamics could also be due to conflicting reports in literature, discussed in detail in Chapter 3.

### Mathematical Basis of Post Processing Techniques

With these advanced imaging techniques, advanced post-processing methods have emerged to allow for novel characterizations of CSF dynamics as well as neural tissue motion dynamics induced by the cardiac cycle. While CSF dynamics have been studied since the late 1990s', neural tissue motion dynamics are a more recently derived parameter of interest. Using analysis techniques for deriving cardiac tissue displacement and strain [12], neuro-engineers have begun looking at displacement and bulk motion of neural tissue to better understand the poorly defined pathophysiology of CMI. To do this using PC MRI techniques, velocity-encoded images taken over the cardiac cycle can be integrated for displacement of a region of interest (ROI) and the peak-to-peak bulk motion of any ROI. More specifically, PC MRI images can be velocity encoded such that a chosen encoding velocity sets the upper and lower bounds of the output velocity information. These PC MR images have a known minimum pixel value of 0, and a maximum pixel value defined by the scanning protocol, which can be linearly transformed as follows:

Based on the linear transformation (2.1):

$$y = mx + b \quad \text{Equation 2.1}$$

with slope,  $m$ :

$$m = \frac{x_2 - x_1}{y_2 - y_1} = \frac{+Venc - (-Venc)}{\text{max pixel value} - 0} \quad \text{Equation 2.2}$$

and y-intercept,  $b$ :

$$b = -Venc \quad \text{Equation 2.3}$$

such that:

$$velocity \left[ \frac{cm}{s} \right] = \frac{2 * V_{enc}}{max \text{ pixel value}} * (Pixel \text{ Value}) - V_{enc} \quad \text{Equation 2.4}$$

Shown graphically in **Figure 2.3**.

With velocity values for each pixel, at every time step, we can then apply kinematics to integrate velocity for displacement based on the following mathematical relationship:

$$velocity = \frac{\Delta \text{ displacement}}{\Delta \text{ time}} \therefore \Delta \text{ displacement} = velocity * \Delta \text{ time} \quad \text{Equation 2.5}$$

Wherein  $\Delta$  represents change, as in the change in time in seconds and change in displacement in centimeters, which allows the following:

$$displacement [cm] = \int_{t_1}^{t_2} velocity \left[ \frac{cm}{s} \right] dt \quad \text{Equation 2.6}$$

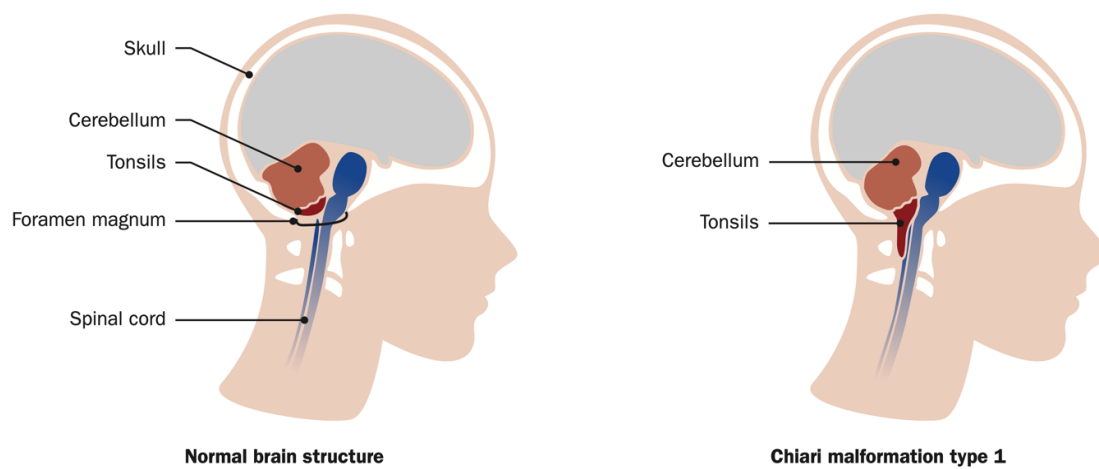
This displacement can be derived for any region of interest (ROI) within the brain with careful ROI selection to ensure no pixels containing CSF are selected. Due to the high velocities associated with CSF movement compared to tissue it surrounds, inclusion of CSF within an ROI could significantly alter results. Displacement of neural tissue induced by the cardiac cycle can also be derived with displacement-encoding imaging techniques, wherein displacement is directly encoded for by the encoding gradient in the MRI pulse sequence. Displacement-encoding imaging, or DENSE (Displacement ENcoded Simulated Echoes) imaging, allows for a greatly improved image resolution and tissue motion quantification down to the submillimeter level [13]. The novel quantification of cardiac induced neural tissue motion at the submillimeter level could provide an improved basis for understanding the underlying CMI pathophysiology in terms of bulk tissue motion parameters.

## Tables

**Table 2.1.** Symptoms of CMI [3]

<b>CSF Obstruction</b>	<b>Compression of Brainstem, Cerebellum, or Cranial Nerves</b>	<b>Spinal Cord Dysfunction (syringomyelia)</b>
<p>Valsalva- or strain-induced occipital/upper cervical pain/headache</p> <p>Hydrocephalus</p>	<p>Swallowing difficulty/choking/aspiration, dysphagia</p> <p>Hoarseness/dysarthria</p> <p>Absent gag reflex</p> <p>Downbeat nystagmus</p> <p>Truncal ataxia</p> <p>Tinnitus</p> <p>Vertigo/dizziness</p> <p>Autonomic symptoms (syncope, drop attacks, sinus bradycardia)</p> <p>Trigeminal/glossopharyngeal neuralgia</p> <p>Trigeminal sensory loss</p> <p>Tongue weakness/deviation</p> <p>Palatal weakness</p>	<p>Upper motor neuron signs</p> <p>Lower motor neuron signs</p> <p>Pain and temperature sensory loss</p> <p>Spasticity</p> <p>Scoliosis (primarily thoracic levoscoliosis)</p> <p>Motor weakness</p>



**Figures**

**Figure 2.1.** In the normal brain, the tonsils stay above the foramen magnum. In Chiari malformation type I, the tonsils descend into the upper cervical canal (the top of the neck) [7].

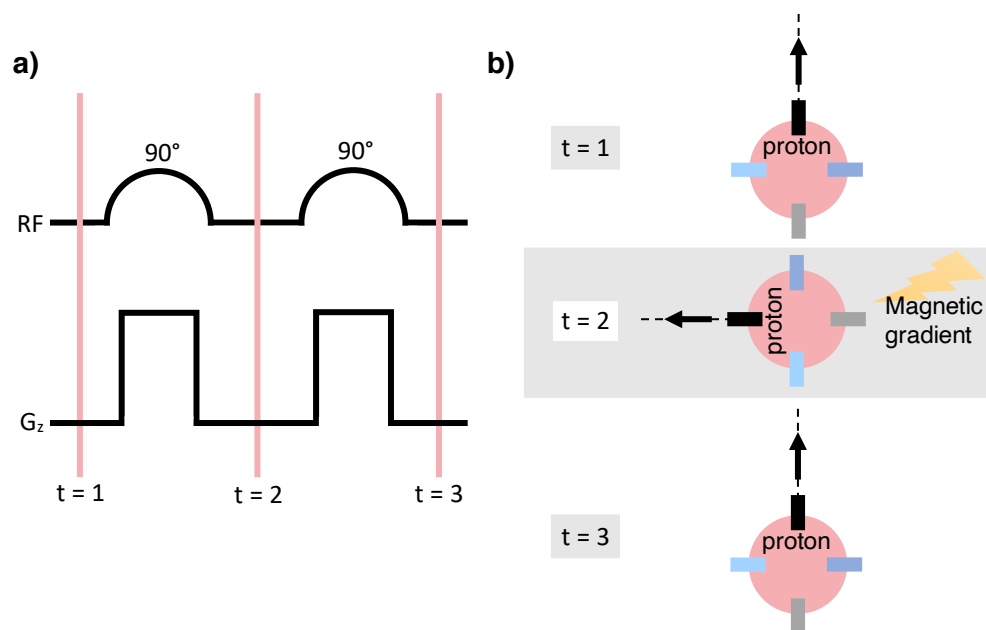


**Figure 2.2. a)** Exemplary portion of a theoretical pulse sequence diagram for a spin echo MRI with  $90^\circ$  radio frequency pulses (RF) and some positive gradient that could represent such things as slice-select, frequency encoding, displacement encoding, etc. **b)** Corresponding orientation of protons before and after application of magnetic gradient (RF pulses here) based on the timing indicated in the pulse sequence diagram in **(a)**.

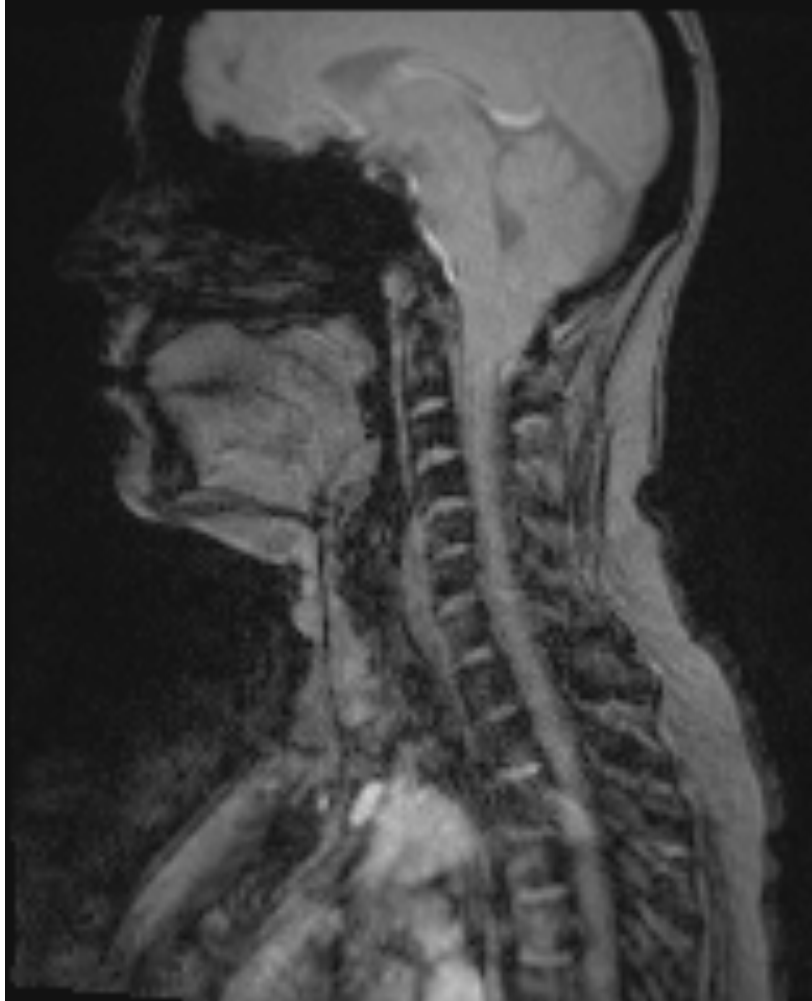


**Figure 2.3.** Example phase contrast magnetic resonance image (PC MRI) of Chiari patient at a mid-point in the cardiac cycle.

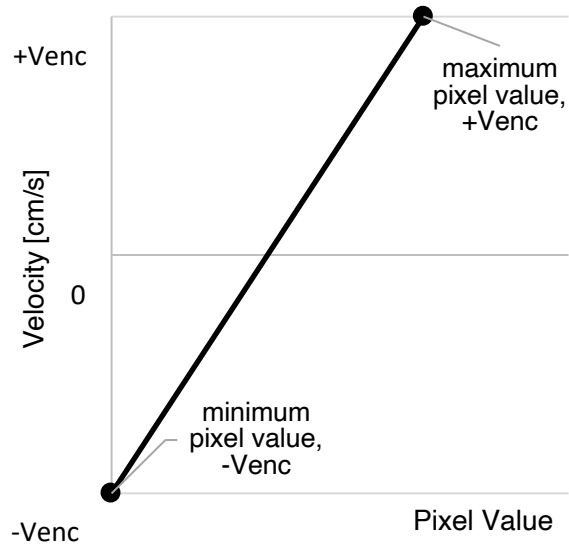


**Figure 2.4.** Graph depicting linear transformation of PC MRI image into velocity data.

## **Chapter 3: In Vitro Evaluation of Cerebrospinal Fluid Velocity Measurement in Type I Chiari Malformation: Repeatability, Reproducibility, and Agreement using 2D Phase Contrast and 4D Flow MRI**

Williams, G., Thyagaraj, S., Fu, A. *et al.* In vitro evaluation of cerebrospinal fluid velocity measurement in type I Chiari malformation: repeatability, reproducibility, and agreement using 2D phase contrast and 4D flow MRI. *Fluids Barriers CNS* **18**, 12 (2021).

<https://doi.org/10.1186/s12987-021-00246-3>

### **Abstract**

#### *Background*

Phase contrast magnetic resonance imaging, PC MRI, is a valuable tool allowing for non-invasive quantification of CSF dynamics, but has lacked adoption in clinical practice for Chiari malformation diagnostics. To improve these diagnostic practices, a better understanding of PC MRI based measurement agreement, repeatability, and reproducibility of CSF dynamics is needed.

#### *Methods*

An anatomically realistic in vitro subject specific model of a Chiari malformation patient was scanned three times at five different scanning centers using 2D PC MRI and 4D Flow techniques to quantify intra-scanner repeatability, inter-scanner reproducibility, and agreement between imaging modalities. Peak systolic CSF velocities were measured at nine axial planes using 2D PC MRI, which were then compared to 4D Flow peak systolic velocity measurements extracted at those exact axial positions along the model.

*Results* Comparison of measurement results showed good overall agreement of CSF velocity detection between 2D PC MRI and 4D Flow ( $p = 0.86$ ), fair intra-scanner repeatability (confidence intervals  $\pm 1.5$  cm/s), and poor inter-scanner reproducibility. On average, 4D Flow measurements had a larger variability than 2D PC MRI measurements (standard deviations 1.83 and 1.04 cm/s, respectively).

*Conclusion* Agreement, repeatability, and reproducibility of 2D PC MRI and 4D Flow detection of peak CSF velocities was quantified using a patient-specific in vitro model of Chiari

malformation. In combination, the greatest factor leading to measurement inconsistency was determined to be a lack of reproducibility between different MRI centers. Overall, these findings may help lead to better understanding for application of 2D PC MRI and 4D Flow techniques as diagnostic tools for CSF dynamics quantification in Chiari malformation and related diseases.

## Introduction

The dynamic movement of cerebrospinal fluid (CSF) has long been the subject of scientific investigation, and its important functional role to support central nervous system health is increasingly realized. For this reason, non-invasive phase contrast magnetic resonance imaging (PC MRI) quantification of CSF dynamics has been pursued for diagnosis, prognosis, and treatment of neurological diseases such as hydrocephalus [14, 15], Chiari malformation [16], and syringomyelia [17, 18]. Variabilities in CSF dynamics, such as increased CSF velocities and/or flow rate, are thought to be indicative of Chiari malformation and related neurological disorders [19, 20]. Single-plane two-dimensional, through-plane encoded PC MRI (2D PC MRI) and time-resolved three-dimensional velocity encoded PC MRI (4D Flow) are promising modalities that allow for CSF dynamics characterization. 2D PC MRI is one of the best known non-invasive methods and currently the only method for both qualitative and quantitative CSF characterization [21]. Clinical application of 2D PC MRI is widely varied with use in visualizing morphological and functional alterations in normal pressure hydrocephalous patients as well as CSF flow assessment in Chiari malformation populations with and without syringomyelia [22]. 4D Flow has shown potential to advance in vivo assessment of complex hemodynamic and CSF flow patterns [23-25]. Originally developed for cardiovascular applications [26], 4D Flow has been applied to analyze CSF velocity differences between healthy controls and Chiari malformation patients, with and without syrinx formation [27]. Contrast-enhanced MRI techniques have also been applied to quantify relatively slow timescale transport phenomena, such as CSF solute transport in humans [28-30]. Additionally, MRI has been applied to quantify short timescale phenomena such as dynamic motion of CSF due to respiration and other maneuvers using real-time PC MRI [31-34] and time-slip MRI [35, 36]. These methods show promise to help reveal new insights about CSF system physiology in health and disease.

At present, the diagnostic relevance of PC MRI-based measurement of CSF velocity dynamics remains under debate by the medical community. For example, the recently published National Institutes of Health common data elements (CDEs) for Chiari malformation clinical research does not include any recommended measurements related to CSF dynamics [37]. The lack of adoption of CSF dynamics as a standard measure for Chiari malformation is likely due to the conflicting findings reported in previous studies comparing CSF velocities in Chiari malformation patients and healthy controls [38-41]. For example, some investigators report elevated CSF velocities in Chiari malformation patients' pre-surgical treatment, and others reported decreased pre-surgical CSF velocities in Chiari malformation patients compared to post-surgery. Also, there are conflicting reports of both elevated and decreased CSF velocities in

healthy subjects compared to Chiari malformation patients. These conflicting findings were discussed in a review by Shaffer et al. [19].

To address the need for improved CSF dynamics quantification, the present study aims to quantify the agreement, reproducibility, and repeatability of 4D Flow and 2D PC MRI measurement of CSF velocities at the craniovertebral junction. Our focus was the craniovertebral junction CSF velocities because these velocities are thought to potentially be a diagnostic indicator of Chiari malformation. To mitigate normal physiological variation in CSF velocities, our approach utilized a subject-specific high-resolution 3D printed model of a Chiari malformation patient with computer controlled pulsatile CSF pump [42]. We hypothesized that 2D PC MRI and 4D Flow would have strong measurement agreement, repeatability, and reproducibility.

### Literature Review

We conducted a meta-analysis of all CSF velocity quantification studies applied in Chiari malformation (**Table 3.1**). These studies show a range of peak CSF velocities in healthy controls and Chiari patients depending on the measurement position along the spine, voxel size, slice thickness, and number of phases. **Figure 3.1** provides a summary of **Table 3.1** results in terms of the average CSF velocities reported in the studies at each axial slice position along the spine (FM to C5) for healthy subjects (N = 91 included across all studies analyzed) and Chiari malformation patients that have not received decompression surgery (N = 166 included across all studies analyzed). **Figure A.1, Appendix A**, contains Forest plots depicting the meta-analysis for each imaging methodology and treatment group, showing the spread of reported peak systolic CSF velocities. This meta-analysis shows peak CSF velocities are elevated in Chiari malformation compared to healthy subjects and the axial position of greatest CSF velocity elevation is most commonly reported at the FM - C1 vertebral level (**Figure 3.1**). However, the standard deviation of peak CSF velocities is considerable compared to group differences and this variance makes specification of a diagnostic threshold for patients versus controls difficult. Notably, several studies included in the meta-analysis had Chiari cohorts with syringomyelia, which is known to affect CSF dynamics [27]. The comorbidity of Chiari and syringomyelia complicates the assessment of Chiari CSF dynamics and requires further investigation to accurately describe the contributions of Chiari and syringomyelia to the CSF dynamics.

Reproducibility and repeatability of CSF velocity measurements, measured in cm/s for individual voxels collected for a region of interest at the craniocervical junction, have not been specifically investigated. A number of studies have been conducted on the reliability of arterial



hemodynamics using 4D Flow [43] and 2D PC MRI [44, 45] measurements. However, arterial flow velocities are typically one order of magnitude greater than CSF velocities. Thus, the reproducibility / repeatability results from these arterial hemodynamics studies are difficult to apply for CSF velocities. Repeatability of 2D PC MRI CSF and cerebral blood flow ( $\text{mm}^3/\text{s}$ ) measurements have been investigated and shown to have moderate in vivo test-retest repeatability [46]. In that study, the authors did not quantify reliability of CSF velocity measurement ( $\text{cm/s}$ ) that has been a focus of interest for CSF-based Chiari malformation diagnostic tests. Repeatability of in vivo 2D PC MRI measurements of CSF flow at the aqueduct of Sylvius has been examined and found to have moderate repeatability [46]. However, aqueductal CSF velocities are typically greater than at the craniocervical junction. Also, the CSF space geometry at the craniocervical junction is more complex than the tube-shaped aqueductal geometry. The craniocervical junction anatomy is an annulus shape that contains spinal cord nerve roots, neuroaxis curvature, and tonsillar descent in Chiari malformation patients. Poor 4D Flow accuracy has been found during timeframes corresponding to low CSF flow rate [47], but further research is necessary before clinical application is feasible.

While many studies have previously quantified repeatability and operator effects for PC MRI hemodynamic and cerebral blood flow characterization [48-55], few studies have quantified these parameters for PC MRI CSF dynamics characterization (**Table 3.2**). Overall, these previous CSF dynamics studies are stratified into focuses on the cerebral aqueduct, the spinal subarachnoid space (SAS), and the C2-C3 area and are summarized in **Table 3.2**. These studies consistently reported strong intra/inter operator agreement and peak velocity measurements are independent of the operator, therefore intra/inter-operator effects are null in this context and were not investigated. A study by Tawfik et al. [56] detailed 2D PC MRI measurement repeatability at the cerebral aqueduct and reported a peak velocity standard deviation of 1.9  $\text{cm/s}$ , which is comparable to the 1.83  $\text{cm/s}$  peak velocity standard deviation we found in the cervical spine (**Table 3.2**). In vivo studies by Sakhare et al. [46] and Luetmer et al. [57] reported standard deviations of 2D PC MRI CSF flow between 0.04 and 0.98  $\text{mL/s}$  but did not look at peak velocity values. Pahlavian et al. [47] performed an accuracy study on 4D Flow quantification of CSF dynamics using a 3D printed in vitro model similar to the one used here and found fairly high accuracy (95% CI  $\pm 1.8$   $\text{cm/s}$ , **Table 3.2**) but did not quantify repeatability nor reproducibility of measurements. These accuracy results from Pahlavian et al. were of similar range as the reproducibility results of this study. To our knowledge, this is the first study to specifically detail the agreement between 2D PC MRI and 4D Flow quantification of peak CSF velocities and characterize reproducibility of measurements across different scanners.

The large variance in CSF velocities reported in Chiari malformation patients versus controls (**Figure 3.1**) in literature is likely due to the wide range in PC MRI acquisition methods and post-processing techniques. Factors contributing to inconsistency in PC MRI measurement results can be summarized as follows: (1) human error introduced by operator region of interest selection and variance of measurement location particularly with 2D techniques [58], (2) inconsistency in eddy current offset correction [47], (3) spatial resolution of MRI slices [21], (4) temporal resolution of number of phases sampled per cardiac cycle [59], (5) transient impact of respiration on time-average CSF flow measured by PC MRI [31, 34, 35] (6) Orientation of the neck angulation [60], (7) normal physiological variance in CSF flow [61], (8) noise and other imaging artefacts generated from subject motion in the MRI scanner [47, 58, 60, 62], (9) respiration-induced  $B_0$  variations [63].

## Methods

### *Study Design*

Experiments were performed using an in vitro subject-specific CSF flow model of a Chiari malformation patient that was tested at five different MRI scanners at four different scanning centers. The centers were physically located as follows: Center 1, University Hospital in Cologne Germany (3T Achieva, Philips Healthcare, Best, Netherlands); Center 2, Emory University in Atlanta, Georgia, U.S.A (Siemens 3T PrismaFit, Atlanta, Georgia, U.S.A); Center 4, University Hospital in Basel Switzerland (3T, MAGNETOM Prisma, Siemens Healthcare, Erlangen, Germany); Centers 3 and 5 were both located at University Hospital in Lausanne Switzerland (3T PrismaFit and 3T Tim Trio, respectively, Siemens Healthcare, Erlangen, Germany). To quantify repeatability, the flow model was scanned three times at each center using both 2D PC MRI immediately followed by 4D Flow MRI. To quantify reproducibility, results were compared across the five centers. Agreement between 2D PC MRI and 4D Flow CSF velocity measurements were also quantified. Results were statistically analyzed within and across MRI centers and between measurement techniques using a linear mixed effects model.

### *Subject Specific In Vitro CSF Flow Model and Experimental Set-up*

To control a consistent CSF flow waveform and anatomic shape across MRI measurement centers, we utilized a computer-controlled in vitro model CSF flow system previously developed by our research group [64] (**Figure 3.2a**). The model was designed based on T2-weighted anatomical MRI data collected for a five-year-old Chiari malformation patient with 6.8 mm cerebellar tonsillar descent below the foramen magnum (FM), as described in Bunck et al. [27]. The spinal subarachnoid space was manually segmented from the medulla to the upper

thoracic spine based on the T2-weighted images. Dorsal and ventral spinal cord nerve rootlets (NR) were added to the model segmentation based on ex-vivo anatomic measurements of nerve root location, radicular line, and descending angle. The model was printed by stereolithography with a spatial resolution of 75  $\mu\text{m}$  (see **Figure 3.2b** for model dimensions).

4D Flow images were acquired to quantify the subject-specific CSF flow waveform in the same Chiari malformation patient. CSF flow rate as a function of time was quantified based on a region of interest located at the C2-C3 vertebral level. This waveform was input to an in-house designed computer-controlled oscillatory syringe pump with pulse-trigger output (for MRI cardiac gating). To allow MRI scanning, the syringe output was connected to the in vitro models via polyethylene tubing. The pump was positioned outside of the scanner operating room with tubing connected to the in vitro model through the waveguide. Tubing was taped to the floor and scanner bed during operation to minimize tubing movement / vibrations during operation. Complete details on the in vitro system dimensions and characterization are provided by Thyagaraj et al. [64]. Scanning was repeated three times at each location. 4D Flow measurements from MRI machines are prone to eddy current offsets arising from non-uniformity of magnetic fields, therefore a static fluid body was placed next to the in vitro model during scanning for a post-processing eddy current offset correction. After affixing the static fluid bodies in place, each trial consisted of a 2D PC MRI scan immediately followed by a 4D Flow scan. Between subsequent trials, the model was manually repositioned by approximately a few centimeters within the scanner bed to mimic realistic conditions in clinics. This repositioning was to mimic the altered position that may occur if a human subject were to be re-scanned in the scanner bed with slightly different body orientation.

#### *In Vitro Imaging Protocol*

Imaging parameters were chosen to represent standard clinical procedures such that these results best represent the repeatability and reproducibility seen clinically.

4D Flow and 2D PC MRI images were collected at each center using the following settings (**Table 3.3**), adapted from a previous protocol [64]. We sought to have identical imaging parameters applied across all MRI machines and across the 4D Flow and 2D PC MRI protocol. In brief, 4D flow datasets were collected in the sagittal orientation with velocity encoding of 15 cm/s, prospective gating, 16 phases per cardiac cycle leading to a temporal resolution of 30 ms, repetition time (TR) of 7.5 ms, echo time (TE) of 4.6 ms, flip angle (FA) = 5°, with 1.5 mm isotropic resolution. Prospective gating of the model was based on the heart rate recorded in conjunction with the subject specific waveform collected for the computer-controlled model.

2D PC MRI data was collected at nine axial slice positions along the model located as shown in **Figure 3.3** with distance between axial planes in **Table 3.4**. Total imaging time was approximately 15 minutes for the 4D Flow protocol and ~30 seconds for each 2D PC MRI scan. Slice positions relative to one another (i.e. foramen magnum to C1 vertebral level) was set to be identical across all MRI centers. The 4D Flow acquisition covered the entire region where 2D PC MRI slices were located.

### *MRI Post-Processing*

Both 4D Flow and 2D PC MRI data were post-processed using GTFflow software (version 2.2.4, Gyrotools Inc, Zurich, Switzerland) by a single person at a center core lab. An eddy current offset correction was applied based on the static fluid body placed next to the in vitro model, to offset errors arising from non-uniformity of the magnetic field [65]. The flow field was also inspected and corrected for any aliasing artefacts when present. 2D PC MRI velocity data at each of the nine axial positions was exported as Matlab (version R2014b, Mathworks Inc, Natick, MA) readable files for quantitative comparison of CSF velocities. At each 2D PC MRI slice position, a 4D flow slice was selected and also exported to Matlab. To quantify peak systolic CSF velocity, first the phase corresponding to peak systole was identified using the maximum spatially averaged velocity of all pixels with non-zero velocities, defined as follows:

$$\text{Spatial Average}_i = \frac{\sum_{n=1}^N V_n}{N} \quad \text{Equation 3.1}$$

where  $i$  represents phase number,  $N$  represents total number of non-zero velocities, and  $V_n$  represent the thru-plane CSF velocity for the respective pixel. The peak systolic value was then measured as the pixel within the phase of peak systole having the greatest velocity value.

### *Statistics*

Because trial, scanning center, and scan type could have significant effects, we developed the following linear mixed-effects model for each replicate:

$$y = \beta_0 + \sum_{k=1}^{13} \beta_k x_k + z_1 + \sum_{k=2}^{13} z_k x_k + \varepsilon, \quad \text{Equation 3.2}$$

where  $y$  is the velocity measurement along the spine,  $x_s$  are binary covariates,  $\beta_s$  are the fixed effects, and  $z_s$  the random effects. Specifically,  $x_1$  indicates whether the treatment group is 4D Flow MRI or not, each of the  $x_k$ s with  $k = 2, \dots, 5$  indicates whether the measurement was taken at the  $j$ th scanning center, and each of the  $x_k$ s with  $k = 6, \dots, 13$  indicates whether the

measurement was taken at one of the eight axial positions (C1, C2M, C2B, C3, C4, C5, C6, and C7). In this model,  $\beta_0$  represents the baseline, which is the mean velocity measurement from 2D PC MRI at scanning center #1 at the FM position along the spine. In other words, this model estimates the difference between another scanning center and Center 1, as well as between another axial position and FM. The baseline may also be the overall mean, or another center or axial position. Our analysis aims to test whether the regression coefficient is significantly different from 0; this is the same hypothesis no matter which baseline is chosen. Additionally,  $z$  represents random effects of the scanning centers and axial slice position (note that the treatment of 4D versus 2D is assumed to be a fixed effect and not included in the random effects), which follow a multivariate normal distribution with mean of zero and a symmetric variance-covariance matrix:

$$\mathbf{z} \sim N(\mathbf{0}, \mathbf{\Sigma}), \quad \text{Equation 3.3}$$

where  $\mathbf{z} = (z_1, \dots, z_{13})'$  is the column vector of all the random effects,  $\mathbf{0}$  is a vector of zeros, and  $\mathbf{\Sigma}$  is the variance-covariance matrix. We used the Matlab (Ver. 2019a Mathworks Corp., Natick, MA) function “*fitlme*” to estimate the parameters in this linear mixed-effects model and test whether each of the fixed effect sizes is significantly different from zero. If so, this would indicate a statistically significant impact on the parameter from treatment groups, scanning centers, or axial position of velocity measurements.

Using this linear mixed-effects model, we obtained p-values for the following 14 fixed effect sizes: the baseline (Center 1), scan type (4D Flow MRI or not), scanning centers (Centers 2-5), axial position of measurement (C1, C2M, C2B, C3, C4, C5, C6, and C7). We accounted for multiple comparisons by applying the Bonferroni correction where the threshold for significant p-values was adjusted to be  $\alpha/14$ , where  $\alpha$  is the experimentwise type I error rate.

## Results

MR images were collected over three trials at five scanning centers using 2D PC MRI and 4D Flow. Trial 3 at Center 4 and trial 2 at Center 5 were excluded from analysis due to a bubble detected in the entrance tubing during scanning; all other scanning centers (Centers 1, 4, and 5) had three successful trials for each imaging modality that were included in analysis.

### *Agreement of CSF Velocity Detection by 4D Flow versus 2D PC MRI*

Our statistical analysis concluded that 4D Flow and 2D PC MRI are comparable methods for CSF velocity measurements at any scanning center and for any vertebral position. No

evidence was found indicating disagreement ( $p = 0.86$ , **Table 3.5**) and there was moderate agreement seen in the Bland Altman Plot (**Figure 3.4**). In all, there was an average difference of 0.02 cm/s between measurements of each scan type with a 95% confidence interval (CI) of -0.28 to 0.24 cm/s (**Table 3.5**) and a maximum difference of 2.9 cm/s (**Figure 3.4**). No individual center had perfect agreement between 4D Flow and 2D PC MRI values. While the measurements showed no discernable trend relating to axial position of measurement, relative clusters formed for each scanning center showing that scanning center likely effects velocity measurement. Notably, a linear trend arose wherein the average velocity and difference between imaging modalities linearly decreased from Center 1 to Center 5, sequentially.

#### *Repeatability*

Repeatability within centers was relatively consistent with confidence intervals less than  $\pm 2$  cm/s (15% of the average measured value of 14 cm/s), (**Figure 3.5**). 4D Flow and 2D PC MRI had similar degrees of repeatability, with some centers showing potentially more consistency of 2D PC MRI measurements and some showing better consistency of 4D Flow measurements. Comparatively, Center 2 showed the greatest degree of repeatability (STD = 0.87 cm/s, **Table 3.6**), Center 1 showed the worst degree of repeatability (STD = 1.50 cm/s, **Table 3.6**), and Centers 3 – 5 had relatively moderate repeatability (STD = 1.06 cm/s, 1.18 cm/s, and 1.25 cm/s, respectively, **Table 3.6**).

#### *Reproducibility*

Peak systolic velocities lacked reproducibility across centers. Specifically, Center 2 (CI = -1.26, 0.36 cm/s; **Table 3.5**) and Center 3 (CI = -2.63, 0.29 cm/s; **Table 3.5**) were not significantly different from our baseline, Center 1, (Center 2:  $p = 0.27$ , Center 3:  $p = 0.12$ ; **Table 3.5**) while Center 4 (CI = -3.42, -0.76 cm/s; **Table 3.5**) and Center 5 (CI = -3.23, -1.76 cm/s; **Table 3.5**) were statistically significantly different from baseline (Center 4:  $p = 2.2 \times 10^{-3}$ , Center 5:  $p = 3.3 \times 10^{-10}$ , **Table 3.5**). This lack of reproducibility can be seen in **Figure 3.6**, wherein 4D Flow peak systolic velocity measurements displayed worse reproducibility than 2D PC MRI peak velocity measurements. **Figure 3.4** also depicts this lack of reproducibility, as there is some overlap between Centers 1, 2, and 3 but Centers 4 and 5 are noticeably different. On average, peak systolic velocities at Center 1 were greater than Center 2 through 5, sequentially (**Figure 3.6**). Each center appeared to have a relative offset value of measurements, indicating a calibration factor may be useful in future comparative studies of PC MRI measurement values.

## Discussion

This study quantifies agreement, repeatability, and reproducibility of 2D PC MRI and 4D Flow characterization techniques for the measurement of CSF flow velocities at the craniovertebral junction in Chiari malformation. We found that agreement between 2D PC MRI and 4D Flow was good, repeatability within any one scanner was fair, and reproducibility across centers was poor. An anatomically realistic in vitro CSF flow model was used to conduct experiments performed at five MRI scanning centers. Peak systolic velocities were found to range from 8.3 to 17.3 cm/s, which falls within the range of values reported in Chiari malformation patients (**Table 3.1**).

### *Agreement*

Peak systolic velocity values for 2D PC MRI and 4D Flow had overall good agreement for all centers analyzed with an average difference of 0.02 cm/s with 95% CI of -0.28 To 0.24 cm/s (**Table 3.5**). This finding supports that either technique can be used within a scanning center and the results would be comparable within exact slices. In clinical practice, a specific slice location is required for 2D PC MRI, while the slice location to be analyzed with 4D Flow is selected after image acquisition by re-slicing of the data. This provides added flexibility for analysis of CSF peak velocities that is not possible using 2D PC MRI. Our approach aimed to acquire 2D PC MRI and 4D Flow with similar spatial and temporal resolution (**Table 3.3**). However, it was not possible to identically match all scanner parameters which may have led to some differences in results across protocols.

Notably, variance across measurements was greater in 4D Flow results than 2D PC MRI (STD = 1.83 cm/s and 1.04 cm/s, respectively, **Table 3.6**). 4D Flow datasets seem to be closer to zero on average than the 2D PC MRI datasets yet the 2D PC MRI data has a narrower range of values than the 4D Flow data. That is to say, 2D PC MRI had less variance overall than 4D Flow across centers but failed to accurately estimate the mean as well as 4D Flow, therefore indicating greater precision and less accuracy in 2D PC MRI than 4D Flow measurements (**Figure 3.5**). Without a “Gold Standard” known peak CSF velocity in the in vitro model, the underlying factor leading to this variance requires further research. This technique-based measurement variance can be seen in **Figure 3.4**, where all measurements lie within  $\pm 3$  cm/s. Here, the overall good agreement between the techniques is apparent, but the relative clustering of values based on scanning center reveals an important insight into the reproducibility and repeatability of techniques. These center-based clusters could be due to scanner-specific effects at each center, wherein each scanner has a quantifiable effect on the measurements it makes. With a more

focused research study, these scanner-effects can be understood and potentially mitigated by use of a standardized scanner calibration technique.

### *Repeatability*

Repeatability of measurement values within any scanner was dependent on each individual scanning center. This variance could be due to axial slice location relative to the model anatomy as peak velocity can vary significantly across the caudal brain and cervical spine. The difference in peak CSF velocity across axial positions was found to be significantly different from the foramen magnum (FM) baseline in four of eight locations ( $p < 0.05/14=0.0036$ , **Table 3.5**). Therefore, some variance is expected in the model and will likely be even greater in vivo. **Figure 3.5** provides a visual depiction of the repeatability of either technique in each center where each measurement value was subtracted from the average peak systolic CSF velocity across axial positions for each center. Specifically, the horizontal bars across each box represent the median of each dataset; the closer this median bar is to zero, the better the repeatability within that center for that scanning technique.

### *Reproducibility*

Overall, the most important factor leading to measurement inconsistency in our study was lack of reproducibility across MRI scanning centers. **Figure 3.6** shows that across axial positions, each center tended to have a relative offset based on the specific scanner used. In general, Center 1 reported the highest values for peak systolic CSF velocity followed by each other center sequentially, with Center 5 generally having the lowest reported peak systolic velocity values. This scanner-specific relative offset could be indicative of systemic difference across scanners. As mentioned above, this relative offset at each center is an important source of variance between scanning centers and could potentially be corrected by a standardized calibration procedure. This variance between scanning centers could potentially be due to scanner specific field inhomogeneity, eddy current generated during scanning, and/or inconsistency of the in vitro experimental set up. It is possible to eliminate eddy current offsets in 4D Flow scans by use of a zero-flow condition, whereby the resultant velocity field from that measurement can be applied for correction, but was not done here as this research is clinically oriented and sought to mimic in vivo conditions. Therefore, variance due to eddy current offsets during scanning are expected to be representative of those found in a clinical setting. We sought to reduce the effect of scanner specific field inhomogeneity with post-processing techniques, but it is to be expected in every clinical setting that there will be local magnetic field inhomogeneities and/or gradient imbalances that could be inconsistent over the whole field of view. To mitigate any potential experimental



inconsistency, experiments were conducted with identical conditions across all centers including use of identical tubing, fittings, and computer controlled oscillatory pump and identical control waveform (see Methods). Additional details on the in vitro system are also provided by Thyagaraj et al. [64]. Further, reproducibility varies slightly at different axial positions of imaging. This reproducibility is exaggerated at lower vertebral positions, with statistically significant differences at the C3, C4, C6, and C7 positions. Notably, C7 had the greatest significance ( $p = 9.5 \times 10^{-12} < 0.05 / 14 = 0.0036$ ) and the largest effect size (-2.17, -1.24) of any vertebral position. At higher axial positions, specifically the FM – C2 levels, the difference is not significant. Therefore, we do not believe vertebral position contributed greatly to the lack of reproducibility.

#### *Case Study – Comparison of Centers 2 and 3*

Centers 2 and 3 utilized the same machine and provide an interesting case study, therefore a secondary statistics model was utilized wherein Center 2 was used as the reference rather than Center 1 (**Appendix A, Table A.1**). A statistically significant difference was found between Center 2 and Centers 4 and 5 ( $p = 1.4 \times 10^{-6}$  and  $4.1 \times 10^{-22}$ , respectively); no significant difference was found between Center 2 and Centers 1 and 3 ( $p = 0.27$  and  $0.11$ , respectively). These results show that while Centers 2 and 3 utilized the same machine and had a small amount of clustering (**Figure 3.4**), Center 2 was most similar to Center 1, therefore utilizing the same type of machine does not guarantee how similar results will or will not be. Based on this, scanner calibration procedures should potentially be developed based on individual scanning machines.

#### *Relevance of Findings to Clinical Diagnostics for Chiari Malformation*

A meta-analysis of similar studies in literature and previous investigations of healthy and Chiari CSF dynamics reveal important insights for the clinical application of novel PC MRI peak velocity quantifications in the cervical spine. **Figure 3.1** shows that these previous investigations of CSF dynamics reported consistently elevated peak CSF velocities in Chiari patients compared to healthy controls at every vertebral level, with a maximum difference of 6.9 cm/s at the C1 position. This difference points towards an underlying physiology of Chiari malformation at the C1 vertebral position that could be leveraged for improved diagnostics pending reliable detection, which requires disagreement between groups to be less than the effect size. Good agreement between 2D PC MRI and 4D Flow measurements indicates both methods would be acceptable in clinical use to characterize CSF dynamics. We also found intra-scanner repeatability of either measurement type to be good, but inter-scanner reproducibility was poor. This lack of reproducibility may help us understand previous studies with conflicting results regarding Chiari CSF dynamics. Mitigation of the lack of reproducibility across centers could be achieved with a

standardized calibration procedure such as generating scanner specific reference values for healthy volunteers.

### **Limitations**

Several limitations have been identified within this study, the use of an in vitro model being the primary limitation. To better understand each parameter and its specific effects on measurement variability, a simple model with an analytical solution could be investigated in future studies with varying levels of complexity, though this was not done here as the focus of this research was for Chiari Malformation applications. We utilized an in vitro subject specific model of a pediatric Chiari patient, but in vivo studies are needed to understand the full range of physiologically-rooted variability that can occur such as the impact of respiration, movement artefacts, etc. The use of a pediatric Chiari patient for a subject specific model results in data that is not representative of all conditions and individual anatomies, limiting the application of these results to adult populations and other disease populations. The precise 3D flow field in the in vitro models has not been validated for any specific Chiari patient. This model used one representative flow waveform to control the oscillatory pump, which introduces further specificity of these results and limits a broader application. Importantly, the use of a rigid model here is not realistic to in vivo situations. Rigid model structures do not model tissue properties therefore flow field characteristics of such models cannot be accurately assessed and must be taken into consideration in the application of results shown here. Future studies to detail and develop an in vitro model of these tissue properties are necessary. Depending on the sensitivity of the measurements, the location of the imaging plane can cause error in the results and introduce an operator bias in the data. Operator dependence has been detailed by previous studies [58, 66] and therefore was not included here as a parameter of interest.

This study focused on measurement agreement, repeatability, and reproducibility and did not quantify a “Gold Standard” measurement for quantification of accuracy. While we sought to set up identical experiments at each center for each trial, the computer-controlled oscillatory pump can only control the waveform input to the inlet. Although tubing was relatively rigid, the exact waveform at the model outlet cannot be known without independent quantification. The exact waveform could be quantified by independent measurement of CSF velocities by flow measurement with laboratory bench-top devices but was outside the scope of this study. Finally, the use of computational flow dynamics could be used to further characterize velocity field errors and an accuracy based on the input flow waveform. Computational flow dynamics have been detailed in a study previously done by our group [47] and therefore were not included here.

### **Conclusion**

A patient-specific in vitro model of Type I Chiari malformation was used to quantify agreement, repeatability, and reproducibility of 2D PC MRI and 4D Flow quantification of peak CSF velocities. The single greatest factor leading to measurement inconsistency of peak CSF velocities was lack of inter-scanner reproducibility. Taken in combination, the results help identify sources of error that can be improved to allow better application of CSF velocity detection for medical diagnostic purposes. Overall, both 2D PC MRI and 4D Flow techniques show promise as diagnostic tools to quantify CSF dynamics in Chiari malformation.

## Tables

**Table 3.1.** Literature review of 2D PC MRI (N = 208) and 4D PC MRI (N = 49) in vivo measurements of peak CSF velocities in healthy (H, N = 91) and Chiari malformation patient (P, N = 166) cases (Note: the peak velocities denoted by an asterisk were measured at points/probes and not throughout the axial plane). H\* indicates healthy subjects with a syrinx.

Study	MR sequence	Subject (N) Healthy / Patient	Axial region	Peak reported velocity (cm/s)	In-plane resolution (mm)	Slice thickness (mm)	# of phases per cycle	Venc (cm/s)	MR Scanner
Bunck et al. (2011) [67]	4D PC MRI	H (10)	FM C1 C2	3.6±2.0 3.6±0.8 4.5±1.0	1.5	1.5	12-14	10,15	1.5T Philips Achieva 2.6
		P (2)	C2/C3	19.7 ± 0.2					
Bunck et al. (2012) [27]	4D PC MRI	H (10)	FM C1 C2	3.2 ± 1.0 3.6 ± 0.8 4.0 ± 1.0	1.5	1.5	12-14	20	1.5T Philips Achieva 2.6
		P (20)	FM C1 C2	7.6 ± 5.0 12.8 ± 11.3 8.4 ± 6.9					
Yiallourou et al.(2012) [68]	4D PC MRI	H (3)	FM	5.2 ± 1.8	1.5	1.5	N/R	10	1.5T Philips Achieva 2.6
		P (4)	FM	11.8 ± 9.0				20	
Shah et al. (2011) [69]	2D PC MRI	P (17)	FM to C2 C4	5.6 ± 2.6 7.5 ± 2.4	0.7	5	14	10	N/R
Houghton et al. (2003) [70]	2D PC MRI	H (10)	FM	2.8 ± 1.0	0.7	5	14	10	1.5T scanner
		P (8)	FM	4.0 ± 1.0					
Dolar et al. (2004) [71]	2D PC MRI	P (8)	FM	6.8 ± 5.1	0.7	5	14	10	N/R
Kruger et al. (2010) [22]	2D PC MRI	P (45)	FM	6.3 ± 4.0	0.7	5	14	10	1.5T scanner
Hofmann et al. (2000) [72]	2D PC MRI	H (18)	C2/C3	3.1 ± 1.7*	0.7	5	16	10	1.5T scanner
Iskandar et al. (2002) [73]	2D PC MRI	H (1)	FM	4.2	0.7	5	14	10	1.5T scanner
		P (8)	FM	9.7 ± 2.3					
Rutkowska et al. (2012) [74]	2D PC MRI	P (3)	FM	7.5 ± 3.5	0.7	5	N/R	10	1.5T scanner

Loth et al. (2001) [75]	2D PC MRI	H (1)	C2/C3	4.0	0.7	5	N/R	3-15	1.5T Signa, GE Medical Systems
Cheng et al. (2012) [76]	2D PC MRI	H (1)	C5	2.2*	N/R	5	N/R	N/R	3T Philips Achieva TX
Alperin et al. (2014) [54]	2D PC MRI	H (37)	C2	1.72 ± 0.06	Anisotropic 0.56 x 0.6	5 – 6	32	7 – 8	3T Magnetom Verio, Siemens
		P (36)	C2	1.61 ± 0.05					
Alperin et al. (2015) [77]	2D PC MRI	P (15)	C2	1.93 ± .78	0.56	5	N/R	7 – 8	3T Magnetom Trio, Siemens

**Table 3.2.** Literature review of repeatability, reproducibility, and agreement studies of PC MRI fluid velocity quantification techniques.

Location	Study	In vitro	In vivo	Protocol	Repeatability (STD, $\sigma$ )	Reproducibility	Agreement	Intra-rater	Inter-rater	Accuracy
Cervical Spine	Williams et al. (2020)	x		2D PC MRI	1.04 cm/s	Table 5	Table 5			
				4D Flow	1.83 cm/s					
Cervical Spine	Pahlavian et al. [47] (2016)	x		4D Flow						$\pm 1.8$ cm/s 95% CI
Cerebral Aqueduct	Sakhare et al. [46] (2019)		x	2D PC MRI	0.042 mL/s			0.99 ICC	0.99 ICC	
Cerebral Aqueduct	Luetmer et al. [57] (2002)	x	x	2D PC MRI	0.291 mL/s			6.4% CV	5.4% CV	
Cerebral Aqueduct	Tawfik et al. [56] (2017)		x	2D PC MRI	1.9 cm/s			0.88 ICC	0.88 ICC	
SAS	Sakhare et al. [46] (2019)		x	2D PC MRI	0.981 mL/s			0.94 ICC	0.94 ICC	
Upper C2	Koerte et al. [78] (2013)		x	2D PC MRI				0.881 ICC	0.985 ICC	

**Table 3.3.** MRI protocols used for 2D PC MRI and 4D Flow MRI acquisition.

<b>Parameter</b>	<b>2D PC MRI</b>	<b>4D Flow MRI</b>
Spatial resolution	1.5x1.5x3	1.5x1.5x1.5
FOV [mm]	150x180	150x180x40
Number of heart phases	16	16
Parallel Imaging	no	2
Sym. Enc.	yes	yes
Halfscan	no	0,75/1
Partial Echo	no	no
TR	5.5	7.5
TE	3.9	4.6
Flip angle	10	5
RF Spoiling	yes	yes
Scan Time	32s	14m35s
BW	866	866
VENC	15	15
k-space segmentation factor	2	1
Trigger delay	7 ms	7 ms
Distortion correction	yes	yes

**Table 3.4.** Distance of between axial planes imaged.

<b>Imaging Plane</b>	<b>Distance from FM [mm]</b>
FM	0
C1	12.7
C2M	25.7
C2B	31.2
C3	35.7
C4	44.7
C5	53.7
C6	63.7
C7	72.7



**Table 3.5.** Effect sizes and corresponding p values estimated from the linear mixed-effects model for velocity measurements. The mean effect size is provided, along with the 95% confidence interval (CI). We used Bonferroni correction to account for multiple testing. \* represents statistical significance under Bonferroni correction where  $p < 0.05/14=0.0036$ .

Effect	Effect Size (95% CI) [cm/s]	p value
Intercept (Center 1: 2D PC MRI at FM)	14.16 (13.12, 15.21)	$4.4 \times 10^{-74}$ *
Scan type (4D – 2D)	-0.02 (-0.28, 0.24)	0.86
Center 2	-0.45 (-1.27, 0.36)	0.27
Center 3	-1.17 (-2.63, 0.29)	0.12
Center 4	-2.09 (-3.42, 0.76)	$2.2 \times 10^{-3}$ *
Center 5	-2.52 (-3.23, -1.76)	$3.2 \times 10^{-10}$ *
C1	-0.80 (-1.37, -0.23)	0.006
C2M	-0.49 (-0.96, -0.02)	0.042
C2B	0.01 (-0.46, 0.48)	0.95
C3	-1.21 (-1.67, -0.75)	$6.22 \times 10^{-7}$ *
C4	-1.36 (-1.85, -0.87)	$1.08 \times 10^{-7}$ *
C5	-0.54 (-1.15, 0.07)	0.084
C6	-1.26 (-1.77, -0.75)	$2.0 \times 10^{-6}$ *
C7	-1.71 (-2.17, -1.24)	$9.5 \times 10^{-12}$ *

**Table 3.6.** Standard deviations of scanning centers for scanning type data subsets and over the entire dataset.

	<b>2D PC MRI [cm/s]</b>	<b>4D Flow [cm/s]</b>	<b>Overall [cm/s]</b>
Center 1	1.13	1.58	1.50
Center 2	0.93	0.74	0.87
Center 3	1.00	1.22	1.06
Center 4	0.69	1.38	1.18
Center 5	1.08	0.92	1.25
<b>Overall</b>	1.04	1.83	1.49

### Figures

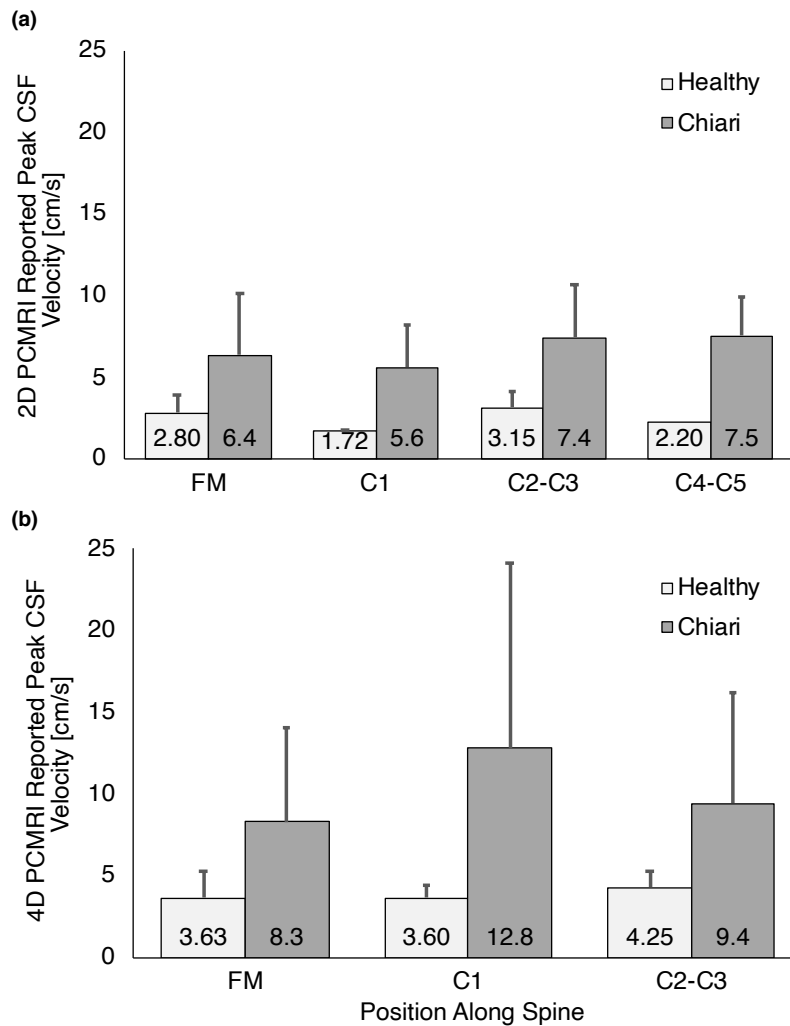


**Figure 3.1.** Summary of the average peak CSF velocities reported in 2D PC MRI (a) and 4D PC MRI (b) literature for healthy subjects and Chiari malformation patients pre-decompression surgery. Average values in figure are weighted by number of subjects within each study. Error bars represent pooled reported standard deviation for studies included in each group. The total number of healthy and Chiari malformation patient studies included is 91 and 166, respectively (see **Table 3.1** for individual values). FM = foramen magnum.

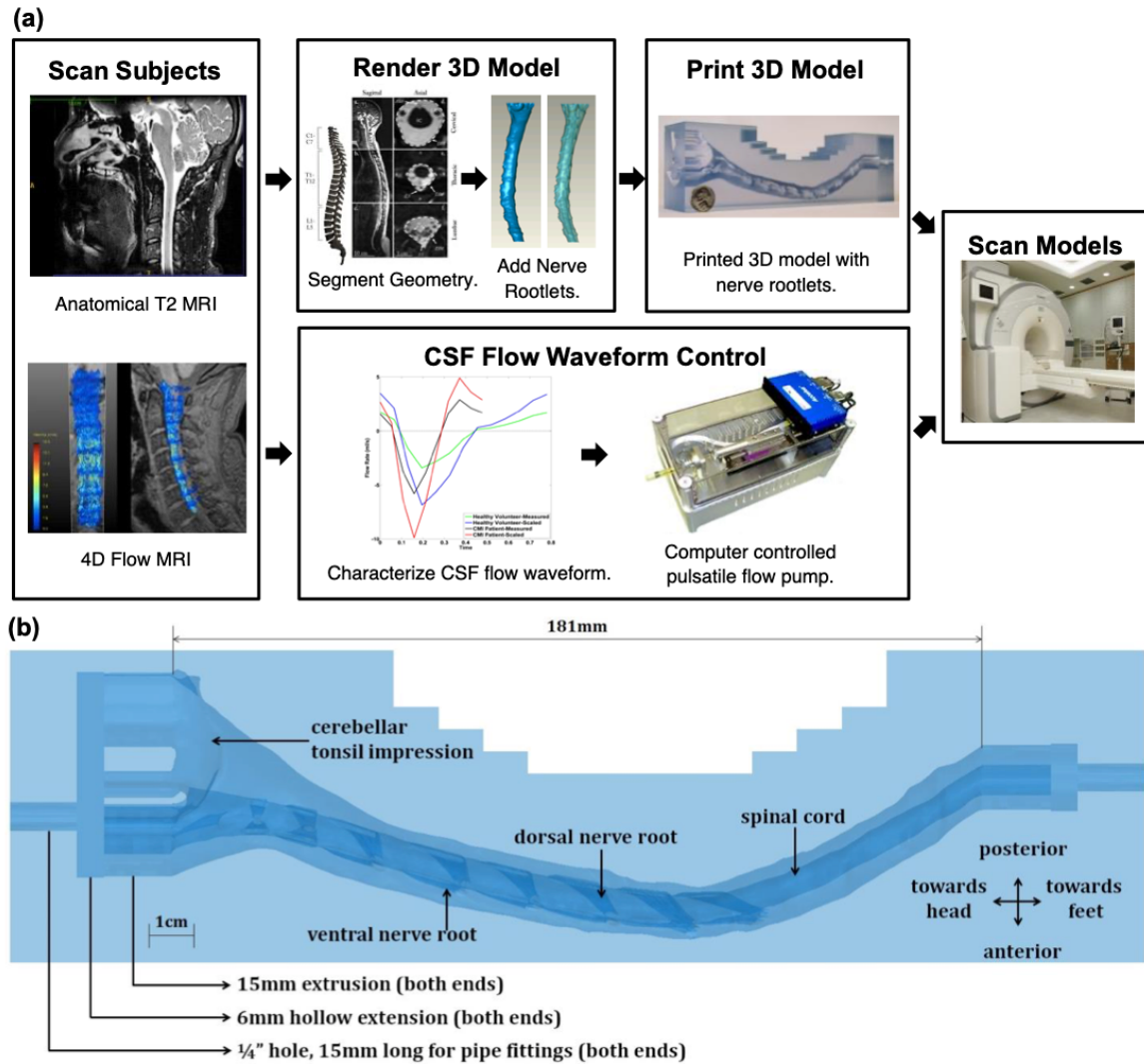


**Figure 3.2.** (a) Development of in vitro models based on subject specific scans. First, subjects were scanned to produce a T2 anatomical MRI and a 4D Flow MRI. The anatomical MRI was then used as a basis for the 3D model. The 4D Flow MRI allows the determination of the cerebrospinal fluid (CSF) flow waveform which informs a computer-controlled pump. The model is then connected to the pump and scanned at each MRI center. (b) Cross section of the completed model.

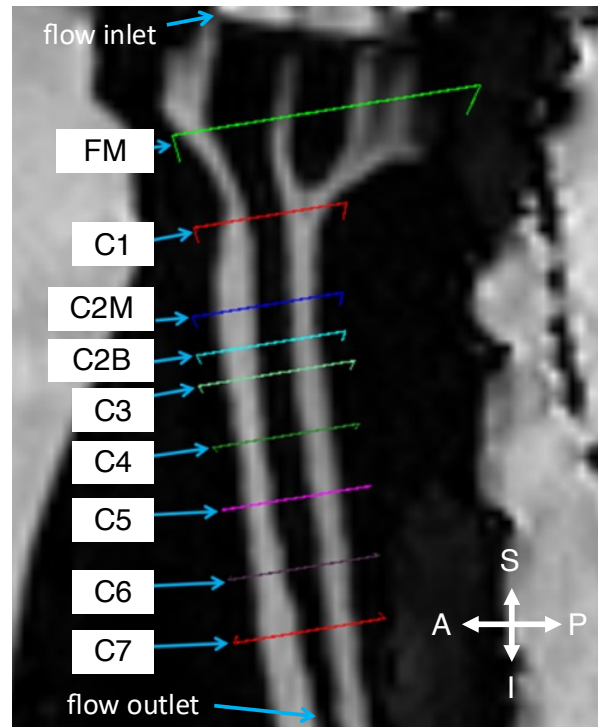


**Figure 3.3.** Axial positions of 2D PC MRI and 4D Flow MRI velocity measurements with flow inlets and outlets indicated. Distance between imaging planes can be found in **Table 3.4**. A = anterior, P = posterior, S = superior, I = inferior; FM = foramen magnum.

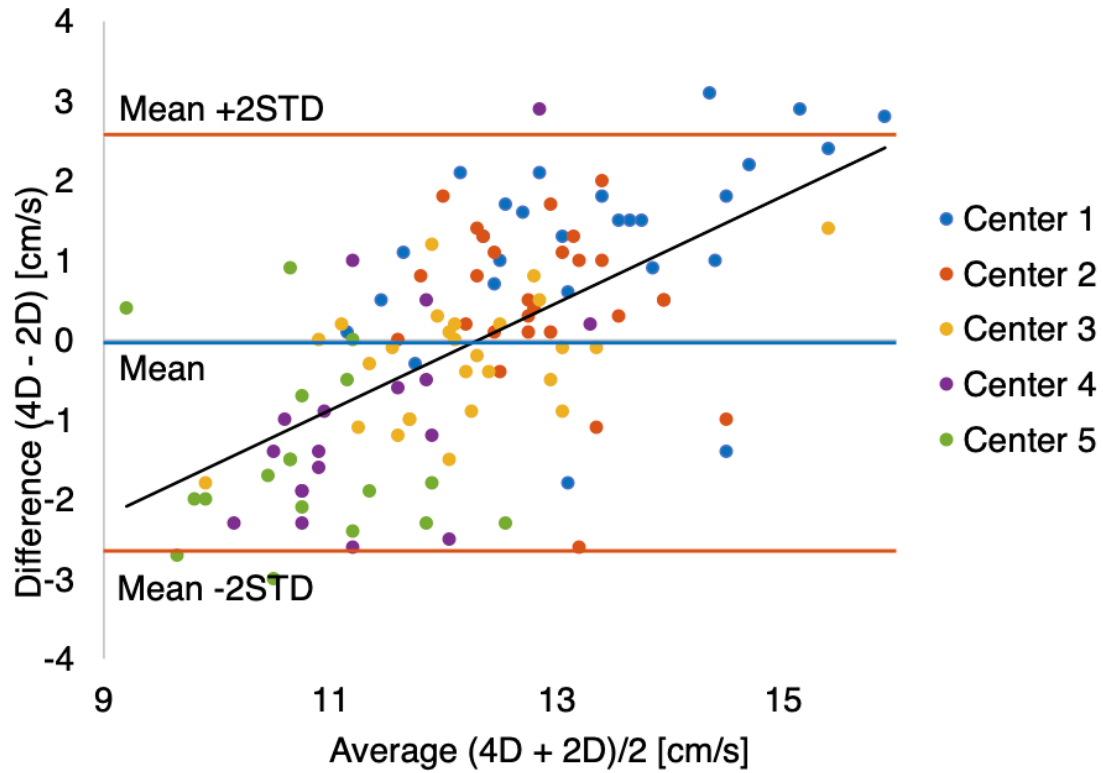


**Figure 3.4.** Bland-Altman plot showing agreement between 2D PC MRI and 4D Flow measurements; the trendline of the data is indicated by the black line, the mean of the differences is shown in blue, and the mean  $\pm 2$ STD is indicated by the red lines.

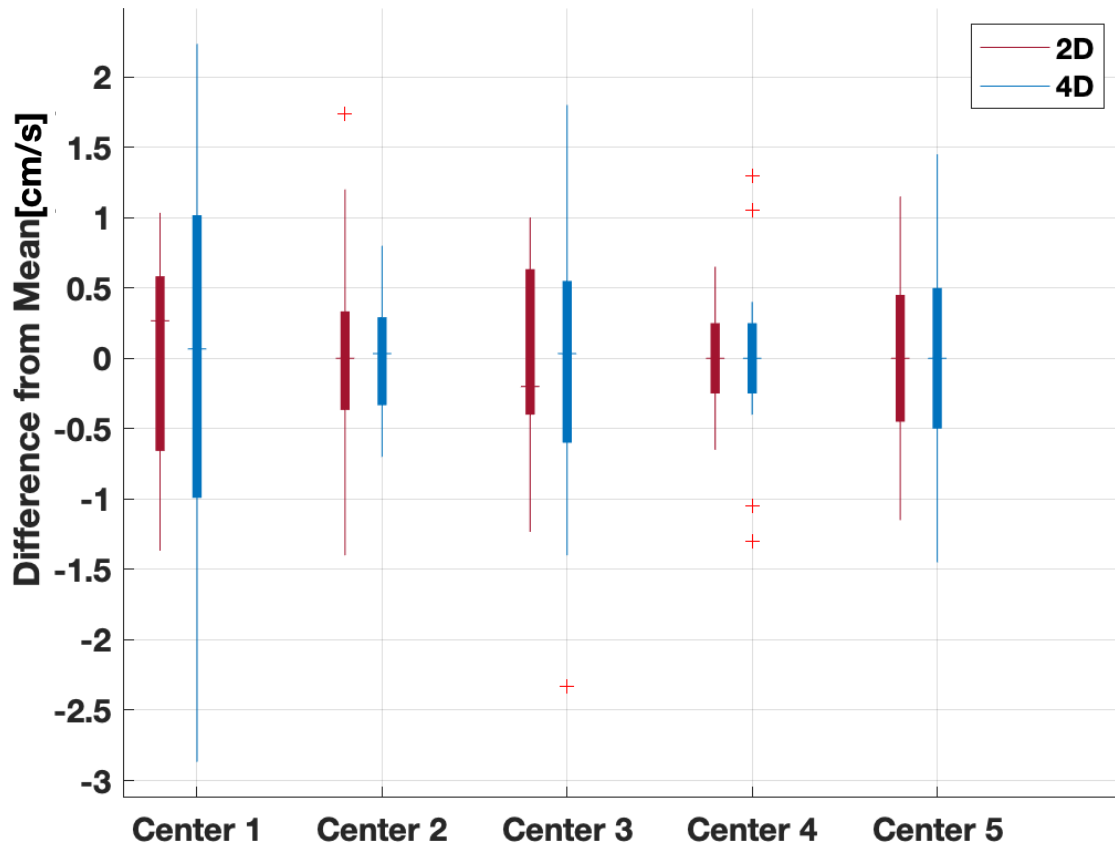


**Figure 3.5.** Box plot showing the difference between average velocity measurement at each axial location and each individual axial velocity measurements at each center. Top and bottom of boxes indicate 25<sup>th</sup> and 75<sup>th</sup> percentile of values with horizontal lines indicating the median of each value set and outliers represented as red cross marks.

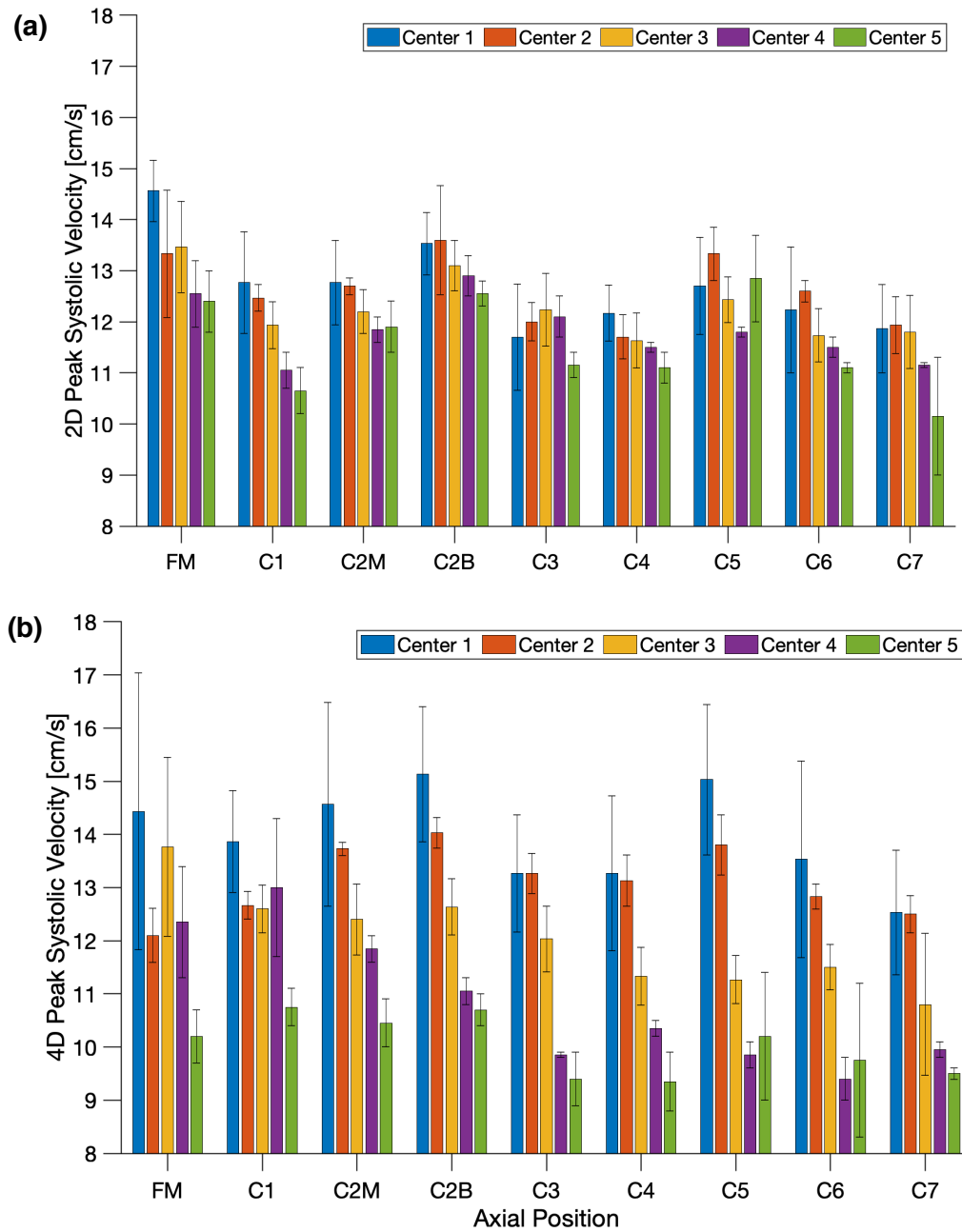


**Figure 3.6.** (a) Peak systolic 2D PC MRI CSF velocity at each axial position for each center. (b) Peak systolic 4D Flow CSF velocity at each axial position for each center. Error bars shown represent standard deviation.



## **Chapter 4: Quantification of Cardiac-Related Neural Tissue Motion in Type 1 Chiari Malformation: A Case Control Study pre- and post-Spinal Decompression Surgery**

### **Abstract**

#### *Objective:*

To evaluate tissue motion relative to two neighboring regions in the craniovertebral junction with 2D PC MRI to test the hypothesis that significant differences exist between the absolute maximum relative motion of the spinal cord in pre- and post-operative type I Chiari Malformation (CMI) patients compared to healthy controls, as well as between CMI patients before and after surgical intervention.

#### *Methods:*

Ten healthy volunteers and ten Chiari patients were scanned using 2D PC MRI to quantify neural tissue displacement of three different regions of interest within the craniovertebral junction. Chiari patients were scanned before and after surgical intervention. Relative tissue motion was then defined as the difference between two regions of interest investigated here and compared across all groups.

#### *Results:*

In the limited cohort analyzed, no statistically significant differences were found in relative neural tissue motion at the craniovertebral junction between any groups ( $q > 0.10$ ) but tonsillar position was found to be significantly different between groups.

#### *Conclusion:*

While the results presented here are limited by the sample size and imaging resolution, there is some evidence that relative tissue motion could be a parameter of interest and should be studied further to better understand the underlying CMI pathophysiology.

## Introduction

Repetitive central nervous system (CNS) tissue motion occurs over 30 million cardiac cycles per year due to intracranial pressure differences from the cerebral blood flow (CBF) and cerebral spinal fluid (CSF). This repetitive tissue motion results in stress acting on the CNS that is complex in terms of both its magnitude and distribution. Over time, stress on the CNS may damage tissue which can manifest symptoms of Chiari Type I Malformation (CMI).

Currently, CMI is a poorly understood disease with diagnostic standards that do not relate to the presence or severity of symptoms that define the disease. CMI has an estimated prevalence in the general population of about one in 1000, but the majority of these cases are asymptomatic [79]. This difference between those diagnosed and those afflicted with symptoms and therefore clinically significant CMI abnormalities is due to a lack of understanding the CMI disease pathophysiology, resulting in a mismatch between those diagnosed and those in need of intervention.

Modern medical imaging techniques, such as magnetic resonance imaging (MRI) cannot directly measure tissue stress non-invasively, but MRI can be used to quantify bulk tissue motion and displacements [13, 80-82]. Some previous studies have quantified neural tissue motion in Chiari malformation patients compared to healthy controls using a variety of MRI methods but many of these studies had limited sample sizes and few compared Chiari malformation patients pre- and post- decompression surgery; these results are shown in **Table 4.1**. These studies are roughly stratified by the imaging region of interest, focusing on either the spinal cord or the cerebellar tonsils. Of the six spinal cord focused studies included here, three found significant differences in reported cardiac-induced neural tissue motion metrics between Chiari patients and healthy controls. Alperin et al. [53] used phase contrast MRI (PC MRI) to quantify bulk motion in healthy controls and Chiari malformation patients at the C2 spinal cord location but did not report a statistically significant difference in spinal cord motion between patients and controls. This same group performed a later study [54] utilizing similar methods and did find a significant difference in peak spinal cord displacement between patients and controls. Similarly, Hofmann et al. [72] and Lawrence et al. [83] used axial PC MRI at the C2 spinal cord location and found a statistically significant difference between the bulk motion of healthy controls and Chiari patients. However, Terae et al. [84] did not find any statistically significant differences in bulk spinal cord motion between healthy controls and untreated Chiari patients. In regard to cerebellar tonsil motion, two of the five studies included here found significant differences between patient populations and healthy volunteers. Pujol et al. [85] used PC MRI and found a statistically

significant difference between bulk motion of the sagittal tonsil in Chiari patients and controls while Leung et al. [86] saw significant differences between patients and controls using cine balanced fast field echo imaging. In contrast, neither Yiallourou et al. [60] nor Cousins et al. [87] found significant differences in sagittal tonsil bulk motion between controls and Chiari patients using Balance TFE and T2 cine loop methodologies, respectively. While six of these thirteen studies included here did show statistically significant differences between treatment groups, there exists no standard quantitative linear metric of motion and no two studies showing significance utilized the same methodologies to do so, which severely limits the application of these results in practice.

At present, cardiac-induced CNS tissue stress cannot be non-invasively measured directly. However, this stress induces tissue motion that can be non-invasively measured by advanced MRI modalities. This study utilized modern MR imaging and post-processing techniques with aims to quantify differences in cardiac-induced neural tissue motion via novel impaction parameters representing relative displacement between neural regions of interest (ROIs). Specifically, we evaluated the relative motion of three different ROIs, the spinal cord, the cerebellar tonsil, and the pons. We tested the hypothesis that significant differences exist between the absolute maximum relative motion of the spinal cord in pre- and post-operative CMI patients compared to healthy controls, as well as between CMI patients before and after surgical intervention. To understand physiological effects of neural tissue impaction, these parameters were compared between Chiari malformation patients and healthy controls, as well as in Chiari malformation patients before and after decompression surgery.

## Methods and Materials

### *Patients*

Approval for this prospective study was granted by the Emory University institutional review board (**Appendix C**) and all subjects gave informed written consent. Ten patients with clinically diagnosed CMI from 18 to 58 years of age with TP  $\geq$  3-5 mm were prospectively enrolled. Patients were required to meet clinical and diagnostic criteria for inclusion in this study. TP was used as an initial screening criterion and the clinical diagnosis was confirmed by the treating surgeon based on all diagnostic information and patient presentation.

Patients and controls were recruited following the methods outline by Lawrence et al. [83]. In brief, patients were recruited from a pool of individuals scheduled to receive imaging or

evaluations for CMI. Controls were recruited from a random pool of individuals without a history of neurological maladies or symptoms. Patients with the following were excluded: craniospinal deformity, Dandy-Walker malformation, Ehlers-Danlos syndrome, spinal fusion, previous decompression surgery, syringomyelia, or additional neurologic disorders. All ten patients received surgical intervention (ten female, age  $39 \pm 24$  years) as treatment for their Chiari malformations. Ten control individuals were included from 18 to 50 years of age with age matched to the patient group (four female, six male; ages  $35 \pm 16$  years). Controls with organ diseases, neurologic conditions, and craniospinal deformity were excluded. Data for all patients with CMI and control individuals were obtained from March 2011 to August 2014. **Table 4.2** summarizes CMI patient clinical presentation.

### *Surgical Technique*

The surgical technique used here is detailed in Lawrence et al [83].

### *In vivo PC-MRI.*

An almost identical MRI protocol was obtained for all patients enrolled in this study. Due to issues with the original volunteer group, a later round of imaging for a new volunteer group resulted in a slightly different pixel spacing for half of the volunteer group. Patients were scanned both preoperatively and postoperatively with a mean postoperative follow-up time of 2.25 months  $\pm$  1.5 months. Mid-sagittal scans with thru-plane (superior – inferior) velocity encoding ( $V_{enc} = 10$  cm/s) and slice thickness of 5-6 mm were acquired of the entire upper spinal cord with imaging planes oriented perpendicular to the CSF flow direction and imaging parameters based on Lawrence et al. [83]. All scans were electrocardiographically triggered with retrospective gating resulting in 128 phases. Scan time was approximately 5 minutes. Images were acquired using a 3T Siemens Magnetom Trio TIM, Siemens Corp., Berlin, Germany).

### *PC-MRI Post-Processing.*

Impaction was quantified as the maximum absolute difference in the average displacement of two different regions of interest (ROIs), specifically between the spinal cord and either the cerebellar tonsil or the pons. Positive impaction values were therefore indicative of the tonsil or pons ROI moving more downwards than the spinal cord at that time point, while a negative value indicates the spinal cord is moving more downwards than the tonsil/pons ROI at that time point; impaction values of zero indicate synchronized movement of the spinal cord and the tonsil/pons. Average displacement of an ROI was based on the integral of the average ROI velocity throughout the cardiac cycle. PC-MRI images were post-processed using an in-house code developed in MATLAB (version 2019a [MathWorks, Natick, Massachusetts, USA]). An

ROI was manually selected with an interactive selection tool in MATLAB (**Figure 1**). Pixels near the edges bordering CSF were omitted.

The average velocity of all pixels within an ROI was computed at each time step then multiplied by the time increment to derive displacement at that time step. Displacement was then integrated using the trapezoidal rule via the *cumtrapz* function in MATLAB (version 2019a [Mathworks]). Displacement results were then stratified into two categories: bulk motion and relative motion. Bulk motion of any one ROI is defined as the peak average displacement for that ROI across the cardiac cycle. Relative motion is defined as the difference in displacements of two separate ROIs, furthered specified as spinal cord impaction, the difference between the spinal cord ROI and the pons ROI, and spinal cord compression, the difference between the spinal cord ROI and the cerebellar tonsil ROI. Peak spinal cord impaction was quantified as the absolute maximum difference between displacement of the spinal cord and the secondary ROI, either the pons or the cerebellar tonsils (**Figure 4.1**). Eddy current offsetting was applied velocities within each ROI to ensure zero average velocity over the cardiac cycle (**Appendix B, Figure B.1**). Systolic synchronization of each data set was performed by shifting the velocity data sets for each ROI based on the local maxima that occurs closest before peak systole as defined by the spinal cord ROI. To find this local maximum, first peak systole is found as defined by the global minima of the spinal cord ROI velocity data. Next, all local minima before this time point are found and the local minima that occurs closest before the point of peak systole is chosen. This pre-peak systole minimum is then used as the point by which each ROI's velocity will be synchronized to. Each individual data set was processed by two separate operators, and each operator repeated the analysis in triplicates. Datasets were analyzed sequentially within a subject group and only repeated after each subject group was analyzed to reduce operator fatigue and bias.

Each ROI was drawn over a magnitude image of that subject. First, the pons ROI was drawn as follows: starting at the superior pontine notch, a straight line is drawn toward the fourth ventricle, then the posterior limit is defined by the anterior edge of the fourth ventricle and the lower limit defined by the inferior pontine notch. Next, the upper spinal cord/lower medulla region was selected as follows: using the C2 vertebral position as the lower limit, the ROI is drawn around the spinal canal, avoiding any cerebellar tonsillar ectopia (if present), and stops at the foramen magnum, the upper limit of the spinal cord ROI.

### *Statistical Analysis*

In our study design, the patients were measured before and after the surgery, whereas the controls were measured only once. We therefore first analyzed the patient data to examine the effect of the surgery, and then separately compared the patients' data before surgery to the controls, as well as the patients' data after surgery with the controls. For each analysis, we analyzed the raw data from the triplicates. We also took the average of the triplicates and analyzed the average data, as taking the average of the triplicates could potentially reduce the noise in the raw measurements.

When analyzing the triplicate data, we developed the following linear mixed-effects model for each parameter in order to account for the variation among the triplicates:

$$y = \beta_0 + \beta_1 x_1 + \beta_2 x_2 + \beta_3 x_3 + \beta_4 x_4 + z_1 + \varepsilon, \quad \text{Equation 4.1}$$

where  $y$  is the parameter of interest,  $\beta$ s are the fixed effects,  $z_1$  is the random effect among the repeated measurements of the same individual, and  $\varepsilon$  is the error term. In addition,  $x_1$  is the treatment,  $x_2$  is the ROI size,  $x_3$  is the age, and  $x_4$  is the sex. The "treatment" variable refers to before versus after surgery when we analyzed the patient data, and patient versus control when we compared the two groups. The last covariate "sex" was omitted when we analyzed only the patients, all of whom are female.

Using the averaged data, we developed the following linear model for each parameter:

$$y = \beta_0 + \beta_1 x_1 + \beta_2 x_2 + \beta_3 x_3 + \beta_4 x_4 + \varepsilon. \quad \text{Equation 4.2}$$

The symbols have the same definitions as above. Note that this model has only fixed effects and no random effects.

In each linear model, we estimated the effect sizes  $\beta$ s and computed their p-values. To account for multiple testing, we applied the q value method [88] to the p-values for the "treatment" and ROI size variables. The p-values for age and sex were excluded from this adjustment, as they were not our interest and their values were generally large.

## Results

MR images were collected for CM-I patients pre- and post- decompression surgery. Pre-operative scanning images for patient 10 were corrupted and post-operative complications with patient 07 resulted in no imaging performed, therefore these subjects were excluded from this analysis, resulting in a final pre-op and post-op patient sample size of  $N = 9$  for comparisons to controls,  $N = 8$  for comparison within patients. All other subjects and controls had successful scans and were included in analysis. Statistically significant results are summarized in **Table 4.3**. All unadjusted p-values and q values can be found in **Table 4.4**.

### *Bulk Tissue Motion*

Bulk tissue motion was defined as the absolute peak displacement for any pixel in an ROI at peak systole and characterized for the pons, cerebellar tonsils, and the lower medulla/upper spinal cord (**Table 4.5, Figure 4.3**). Peak systole was defined as the time point with the greatest spatial average across the ROI. Comparisons between patients and controls, pre-operatively and post-operatively, revealed no significant differences in the peak bulk motion of any ROI. No significant differences in bulk tissue motion were found between patients and controls, pre- nor post-operatively (**Table 4.4**).

### *Spinal Cord Impaction in CMI Patients Compared to Healthy Volunteers*

Results for all subjects are listed in **Table 4.5**; relative tissue motion results for all patients and controls are plotted in **Figure 4.4**. No significant differences in spinal cord – tonsil nor spinal cord - pons impaction were found between patients and controls, pre-operatively nor post-operatively. Absolute peak spinal cord – tonsil impaction was found to have a moderately significant difference ( $p = 0.096 < 0.10$ ) between patients and controls before adjustment of p-values for the false discovery rate, but this difference failed to remain significant after FDR adjustment using the Benjamini-Hochberg ( $q = 0.23$ , **Table 4.4**).

### *Effect of Posterior Fossa Decompression (PFD) Surgery on Tissue Motion*

Bulk tissue motion of the spinal cord, pons, and cerebellar tonsil regions were not significantly different in patients after receiving surgical intervention. Peak spinal cord impaction, the maximum absolute difference in motion between the spinal cord and either the cerebellar tonsils or pons, is reported in **Table 4.5** and depicted in **Figure 4.4**. Differences between patients pre- and post-operatively were minimal and showed no statistically significant differences (**Table 4.4**).

### *Relationship of Spinal Cord Impaction with Tonsillar Position*

Spinal cord impaction results were plotted against cerebellar tonsillar position for each all subjects, both pre- and post-operative patients and controls (**Figure 4.5 a-b**). Mean and standard deviation for tonsillar position for pre-operative patients (N = 8), controls (N = 6), and post-operative patients (N = 9) were  $8.5 \pm 6.0$  mm,  $-1.2 \pm 2.7$  mm, and  $6.7 \pm 4.0$  mm, respectively. Pearson correlation coefficients for average and peak spinal cord impaction parameters generally lacked meaningful correlations (**Appendix B, Table B.1**). Tonsillar position measurements compared between post-operative patient and controls were found to be significantly different across all comparisons of parameters between groups (q value < 0.05, **Table 4.4**).

### *Operator Effect*

Two operators analyzed each data set three separate times with overall good agreement. This overall good agreement between the operators can be seen in **Figure 4.6**, where all but two data points fall within  $\pm 0.12$  mm ( $\pm 2$ STD). Further, regression analysis of each ROI revealed an  $R^2 = 0.97$  for the pons and cerebellar tonsil regions (**Appendix B, Figure B.2**) while the upper spinal cord/lower medullar region had an  $R^2 = 0.57$  (**Appendix B, Figure B.2**).

### *Effect of Averaging Measurements*

Statistical analysis was performed using both the average result of triplicate measurements as well as over each triplicate measurement to identify the effect of averaging on analysis results. Overall, significance had no discernable trend when comparing the use of all measurements versus using averaged values from repeated measurements. Of the 18 comparisons performed here using all three triplicates for statistical analysis, six comparisons showed significance at 0.1 level but only two comparisons were found to be significant when using the averaged result for analysis (**Table 4.4**). Of the two significant comparisons that resulted from both average and triplicate statistical analysis, only one remained significant after FDR adjustment, indicating that any one measurement may not accurately capture the true mean for that subject.

## **Discussion**

Patients and volunteers were scanned using 2D PC MRI and velocity measurements for specific ROIs were integrated for displacement values for characterization of bulk tissue motion parameters and relative tissue motion parameters. Tissue motion results were then compared across patients before and after surgical intervention, as well as between patients and controls, both pre- and post-operatively. In brief, the Benjamini-Hochberg correction for false discovery rates was used to ensure true statistically significant differences are identified among the 21



comparisons made in this analysis. Of these comparisons, statistically significant differences were found among tonsillar position measurements of patients and controls, pre- and post-operatively (**Table 4.4**).

#### *Comparison of Results to Previous Studies*

To our knowledge, this is the first study to quantify relative tissue motion parameters defined by the difference in motion between two regions across the cardiac cycle. We performed a meta-analysis of previous studies that quantified neural tissue motion and found relatively inconsistent results reported across the literature (**Table 4.1**). **Figure 4.7** depicts the results of this meta-analysis for studies that reported comparable metrics, showing that the results found in this study are relatively similar to what appears in literature. Of the 12 studies included here, half reported statistically significant differences between patients before surgical intervention and healthy controls while the other half saw no significant differences in bulk tissue motion. This lack of consistency in results could be due to different methodologies in imaging parameters, location and orientation of imaging planes, or differences in the post-processing image analysis. Notably, Alperin et al. [53, 54] limit errors due to baseline drift with a constraint of net-zero displacement over the cardiac cycle, while the methods used here applied an eddy-current offset by constraining the velocity to net-zero over the cardiac cycle, similarly to Lawrence et al. 2018 [83]. Anatomical location of the imaging planes and orientation can play a significant role as well, as demonstrated by the two studies performed using axial imaging planes both showing significant differences between patients and controls. Of the 10 sagittal studies included, four showed significant differences between patients and controls, and of those four studies, two used 2D PC MRI. This is understandable, as most clinics make use of 2D PC MRI therefore a greater density of studies utilize this clinically relevant methodology and more results with significant differences are reported from 2D PC MRI studies. Without clear indication from previous studies reporting consistently significant differences in bulk tissue motion between CMI patients and healthy controls, it is difficult to conclude that a truly relevant underlying physiology exists within these tissue motion parameters. We speculate that these bulk motion parameters are not sufficient to characterize the important underlying physiologies of tissue motion. To make meaningful comparisons using tissue motion, we propose relative tissue motion as a parameter of interest to better characterize differences in the CMI disease state and understand the underlying CMI pathophysiology.

*Relationship of Neural Tissue Motion and CMI Pathophysiology*

In all, some differences were seen between the relative tissue motion of healthy volunteers and CMI patients wherein the average relative motion was positive in the healthy state and tended to be closer to zero than that seen in the diseased state (**Figure 4.8**). Statistical analysis using a Benjamini-Hochberg correction for false discovery rates did not show any statistically significant differences in peak spinal cord impaction between pre-operative patients and controls, but unadjusted p-values indicate some moderately significant differences between the peak spinal cord-tonsil impaction of untreated patients and controls (**Table 4.5**). This moderate significance indicates that there could be important differences in spinal cord impaction between untreated CMI patients and healthy volunteers, but larger studies are required to confirm this significance.

To further visualize the important differences seen in the CMI physiology, **Figure 4.8** depicts spinal cord impaction with respect to the cerebellar tonsil and the pons for all patients pre-operatively and healthy volunteers. Here, positive impaction values indicate the spinal cord is moving less downwards than the tonsil or the pons, negative impaction values indicate the spinal cord is moving more downwards than the tonsil or pons, and zero impaction indicates that the spinal cord is moving in synchronization with the tonsil or pons. Notably, the absolute peak spinal cord - tonsil impaction values for healthy volunteers tend to be more negative than those of CMI patients pre-operatively. The opposite phenomenon is seen in the peak and average spinal cord - pons impaction results (**Figure 4.8.b**). In the healthy state, we see that as systole occurs and fluids rush from the head towards the feet, this acceleration causes the spinal cord tissue to be pulled downwards with the fluid. This force dissipates within the tissue as you move upwards and less downward forces are exerted at more superior locations in the brain such as the tonsils and the pons. Mechanistically speaking, the spinal cord should then experience the greatest inferior motion of any tissue in the craniovertebral region, followed by the cerebellum, and the least motion would be seen with the pons. These predictions seem to be supported by the impaction of the healthy volunteers over time; wherein the spinal cord moves the most, resulting in the most negative impaction values with respect to the tonsil, and lesser negative impaction values with respect to the pons. In the CMI state, we see that this is not exactly the case. Instead, the crowding at the foramen magnum caused by the herniation of the cerebellum results in a similar motion pattern in both the spinal cord and the tonsil, seen in **Figure 4.8.a**, wherein the average CMI impaction is closer to zero than the healthy state. We postulate that in the CMI disease state, the perivascular transport is being impacted by the FM crowding and therefore exerting forces

onto surrounding tissue and eventually causing CSF leakage into the spinal canal, resulting in syrinx formation.

#### *Future Directions*

The results here show promise in providing an improved diagnostic basis with further research. A greater study cohort differentiating CMI patients with and without syringomyelia, hydrocephalus, and other important co-morbidities, could reveal important insights of the CMI pathophysiology. Further, a study detailing the bulk and relative tissue motion parameters defined here for asymptomatic but radiographically diagnosed CMI patients could provide more conclusive evidence for an improved diagnostic basis. Comparisons of tissue motion parameters between patients before and after various types of surgical intervention at multiple clinic locations would also provide a better understanding of the effects of surgery to improve surgical candidate selection. Longer term studies with multiple follow-ups after surgical intervention to characterize neural tissue motion parameters could improve understanding of long-term effects to improve long-term surgical outcomes and better inform surgical intervention protocols. Finally, a detailed study comparing pre- and post-operative patients to healthy volunteers using different imaging modalities such as motion tracking, 4D Flow, and DENSE could elucidate underlying methodological sources of variances.

#### *Limitations*

The primary limitation to this study is the small sample size. With a small sample size, the false discovery rate when looking at many comparisons can be high, which can make meaningful comparisons difficult to make. The short and inconsistent follow-up times across patients and controls further limits the results presented here, as longer periods before follow-up scans post-operatively could better represent long-term surgical outcomes. Assessment of surgical outcomes, both short and long term, are important to improve surgical candidacy selection and reduce over- and under-treatment, a common problem within the CMI population. Finally, the use of 2D PC MRI is clinically relevant but has limited image resolution which may not be sufficient for truly accurate measurements on a physiologically relevant scale.

#### *Conclusions*

Relative neural tissue impaction may provide a novel physiological basis to determine clinical significance of a Chiari malformation that has not been previously investigated. While the results here do not provide a conclusive basis for this determination, the moderate significance of neural tissue impaction shown here should be explored further.

## Tables

**Table 4.1.** Literature review of previous studies detailing tissue motion at the craniovertebral junction. \* represents studies that found a statistically significant difference between untreated Chiari malformation type I (CMI) patients and healthy controls.

Study	MRI Method	Imaging Plane	Location	Healthy	Patient
Hoffman et al. 2000	2D PC-MRI	Sagittal	C2 spinal cord	0.7 mL/s	1.3 mL/s*
Alperin et al. 2005	2D PC-MRI	Sagittal	C2 spinal cord	0.33 ± 0.13	0.39 ± 0.17
Alperin et al. 2014	2D PC-MRI	Sagittal	C2 spinal cord	0.17 ± 0.05	0.37 ± 0.2*
Pujol et al. 1995	2D PC-MRI	Axial	Sagittal tonsil	16 ± 7 index	46 ± 25 index*
Lawrence et al. 2018	2D PC-MRI	Axial	Upper spinal cord	0.23 ± 0.08	0.53 ± 0.3*
Williams et al. 2021	2D PC-MRI	Sagittal	Upper spinal cord	0.34 ± 0.15	0.39 ± 0.13
Dawes et al. 2019	Balanced fast-field echo MRI	Sagittal	Cerebral tonsil	N/A	0.57 ± 0.14
Yiallorou et al. 2012	Balanced TFE	Sagittal	Sagittal tonsil	None	> Healthy
Terae et al. 1994	Bolus tracking	Sagittal	Spinal cord	None	> Healthy
Leung et al. 2016	Cine balanced fast-field echo	Sagittal	Sagittal tonsil	0.30 ± 0.1	0.79 ± 0.45*
Nwotchouang et al. 2021	DENSE MRI	Sagittal	Brainstem	0.15 ± 0.04	0.3 ± 0.13*
Pahlavian et al. 2018	DENSE MRI	Sagittal	Brainstem	N/A	0.19 ± .05
Cousins et al. 2009	T2 as cine loop	Sagittal	Sagittal tonsil	0.43 ± 0.06	0.57 ± 0.04

**Table 4.2.** Clinically reported symptoms for all patients before surgical intervention.

<b>Clinically Reported Symptom</b>	<b>Number of Patients (%)</b>
Headaches	80%
Sensory arm	30%
Neck Pain	20%
Dizziness	10%
Instability, Gait Disturbance	10%
Swallowing Difficulty	20%
Extremity Pain	10%

**Table 4.3.** Results of statistical analysis using linear mixed effects model (LME) before and after false discovery rate adjustment (FDR). \* represents statistically significant values after adjustment at the 0.10 level.

<b>Parameter</b>	<b>Comparison</b>	<b>Object</b>	<b>unadjusted p value</b>	<b>q value</b>
Peak Impaction	Pre versus Control	Average analysis	0.096	0.27
Tonsillar Position	Pre versus Post	Average analysis	0.004	0.04*
	Pre versus Control	Average analysis	0.004	0.04*
	Post versus Control	Average analysis	0.001	0.04*

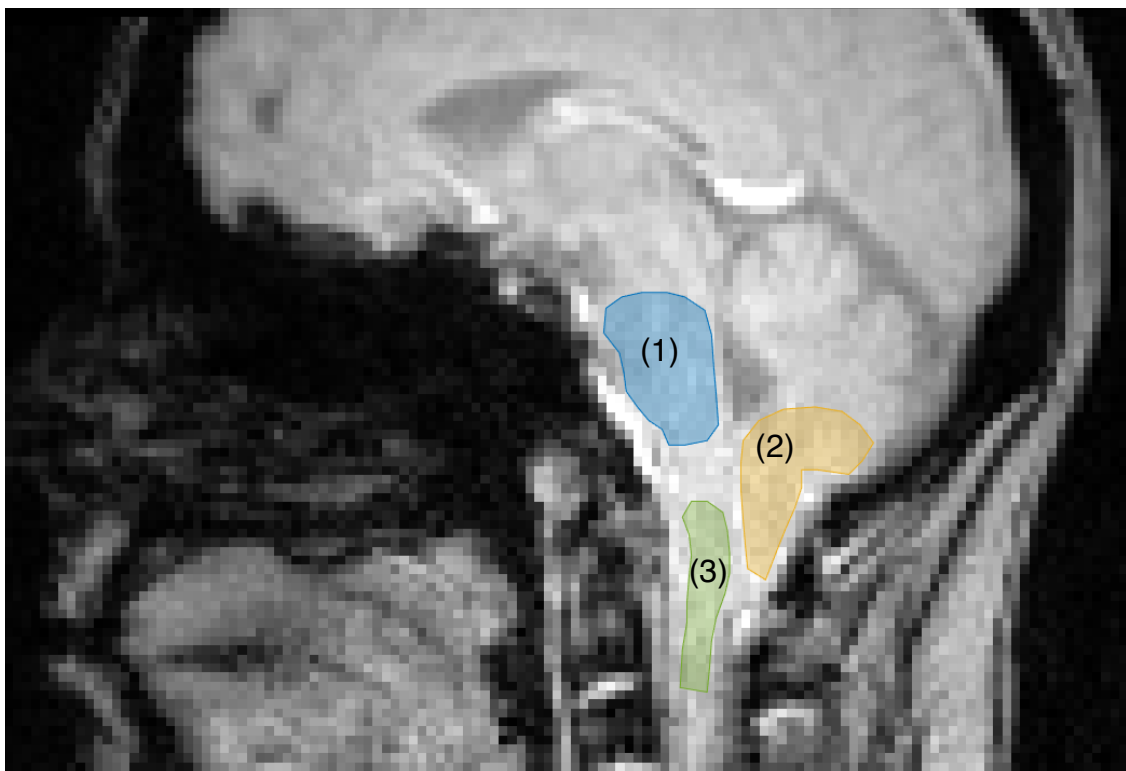
**Table 4.4.** Results of all statistical comparisons across groups, before and after adjustment. \* represent statistically significant results to the 0.1 level.

	<b>Parameter</b>	<b>Triplicate analysis p-value</b>	<b>Triplicate q-value</b>	<b>Average Analysis p-value</b>	<b>Average q-value</b>
<b>Pre vs Post</b>	Spinal Cord	0.71	0.46	0.25	0.42
	Tonsil	0.09*	0.27	0.23	0.42
	Pons	0.95	0.50	0.34	0.45
	Peak Impaction SCT	0.30	0.43	0.41	0.45
	Peak Impaction SCP	0.63	0.46	0.94	0.50
	TP	NA	NA	4.02E-03*	0.04*
<b>Pre vs Control</b>	Spinal Cord	0.88	0.49	0.67	0.46
	Tonsil	0.02*	0.14	0.11	0.27
	Pons	0.50	0.46	0.65	0.46
	Peak Impaction SCT	0.02*	0.15	0.10*	0.27
	Peak Impaction SCP	0.36	0.45	0.47	0.46
	TP	NA	NA	4.02E-03*	0.04*
<b>Post vs Control</b>	SC	0.63	0.46	0.30	0.43
	Tons	0.08*	0.27	0.19	0.39
	Pons	0.97	0.50	0.76	0.46
	Peak Impaction SCT	0.58	0.46	0.85	0.49
	Peak Impaction SCP	0.62	0.46	0.52	0.46
	TP	NA	NA	1.18E-03*	0.04*

**Table 4.5.** Summary of results and descriptive stats for all pre- and post-operative patients and controls.

	<b>Pre-operative</b>	<b>Control</b>	<b>Post-operative</b>
Age (years)	39 ± 24	35 ± 16	39 ± 24
Tonsillar Position (mm)	8.50 ± 6.04	-1.18 ± 2.7	6.65 ± 4.03
Peak Spinal Cord motion (mm)	-0.36 ± 0.13	-0.32 ± 0.11	-0.35 ± 0.18
Peak Tonsil Motion (mm)	-0.16 ± 0.07	-0.15 ± 0.04	-0.17 ± 0.06
Peak Pons motion (mm)	-0.21 ± 0.13	-0.11 ± 0.03	-0.18 ± 0.09
Peak SC - Tonsil Impaction (mm)	-0.16 ± 0.06	-0.22 ± 0.10	-0.19 ± 0.15
Average SC - Tonsil Impaction (mm)	-0.08 ± 0.04	-0.12 ± 0.07	-0.09 ± 0.08
Peak SC - Pons Impaction (mm)	-0.22 ± 0.08	-0.18 ± 0.10	-0.20 ± 0.14
Average SC - Pons Impaction (mm)	-0.11 ± 0.04	-0.10 ± 0.06	-0.10 ± 0.08



**Figures**

**Figure 4.1.** Representative subject p04C scan with regions of interest (ROIs) drawn in: (1) Pons, (2) Cerebellar tonsil, (3) Upper Spinal cord and lower medulla.

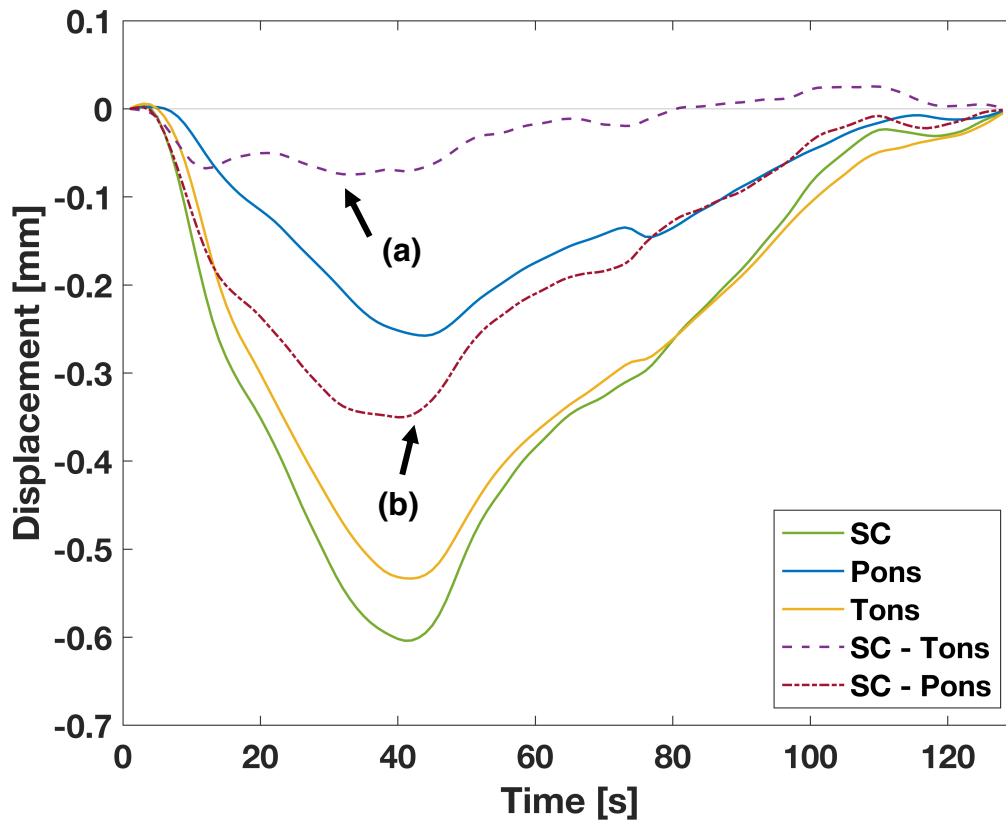


**Figure 4.2.** Displacement and impaction time-series data for representative subject p04C. Solid lines indicate displacement results for specific regions of interest (ROIs), while dotted lines indicate the difference, or impaction, of two ROIs. The points indicated by (a) and (b) represent peak absolute displacement.

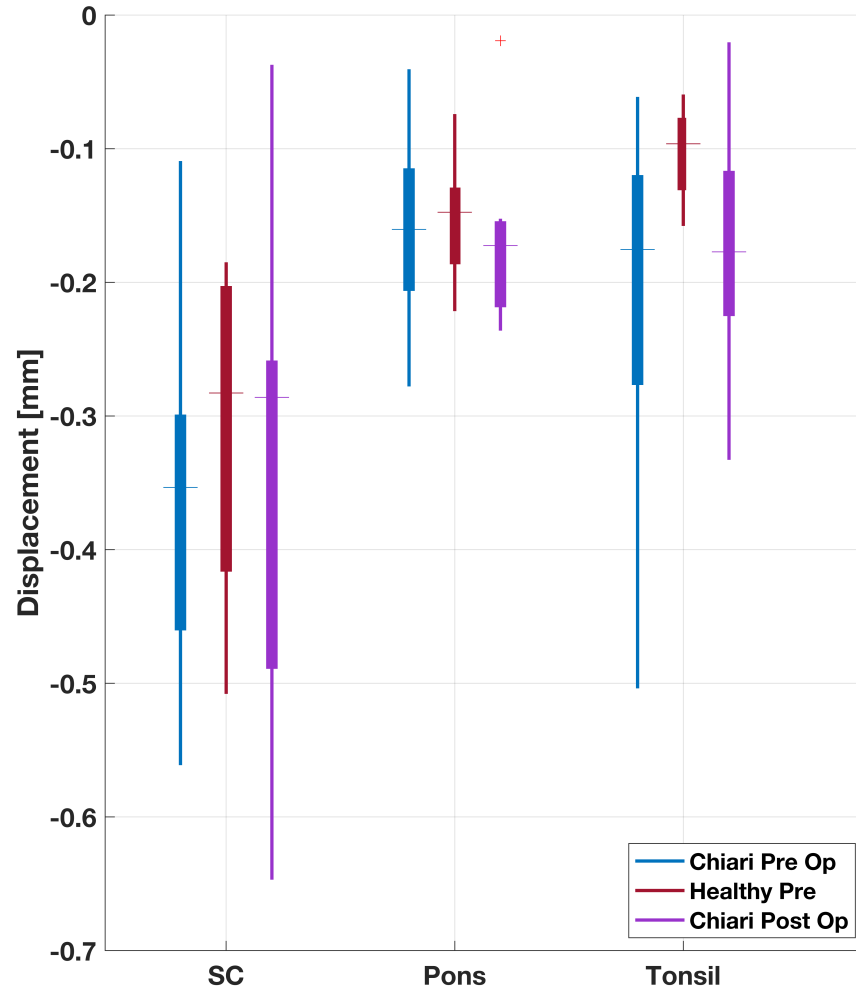


**Figure 4.3.** Peak absolute displacements for all pre- and post-operative patients and controls of each region of interest (ROI). Horizontal bars represent the median value for a dataset, with the upper and lower limits of each box representing the 75<sup>th</sup> and 25<sup>th</sup> quartiles, respectively. Red cross marks represent outliers.

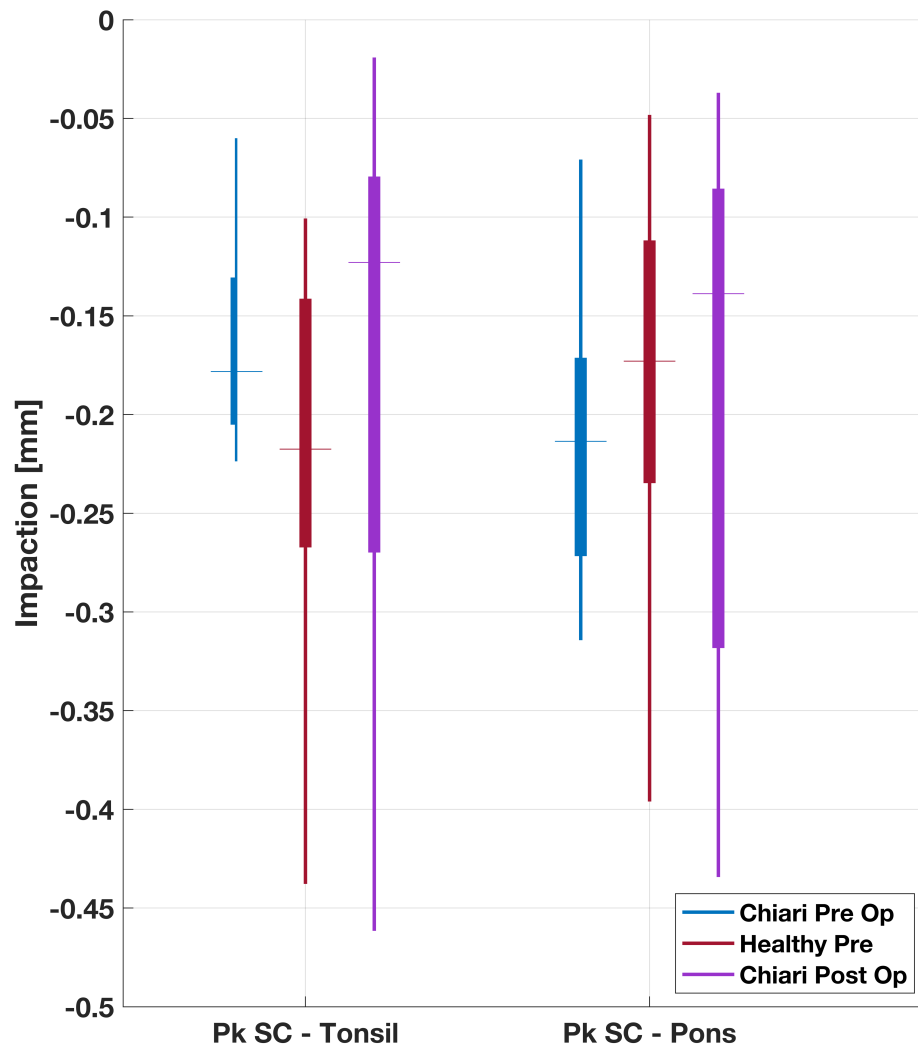


**Figure 4.4.** Peak absolute impaction results for all pre- and post-operative patients and controls of each region of interest (ROI). Horizontal bars represent the median value for a dataset, with the upper and lower limits of each box representing the 75<sup>th</sup> and 25<sup>th</sup> quartiles, respectively. Red cross marks represent outliers.

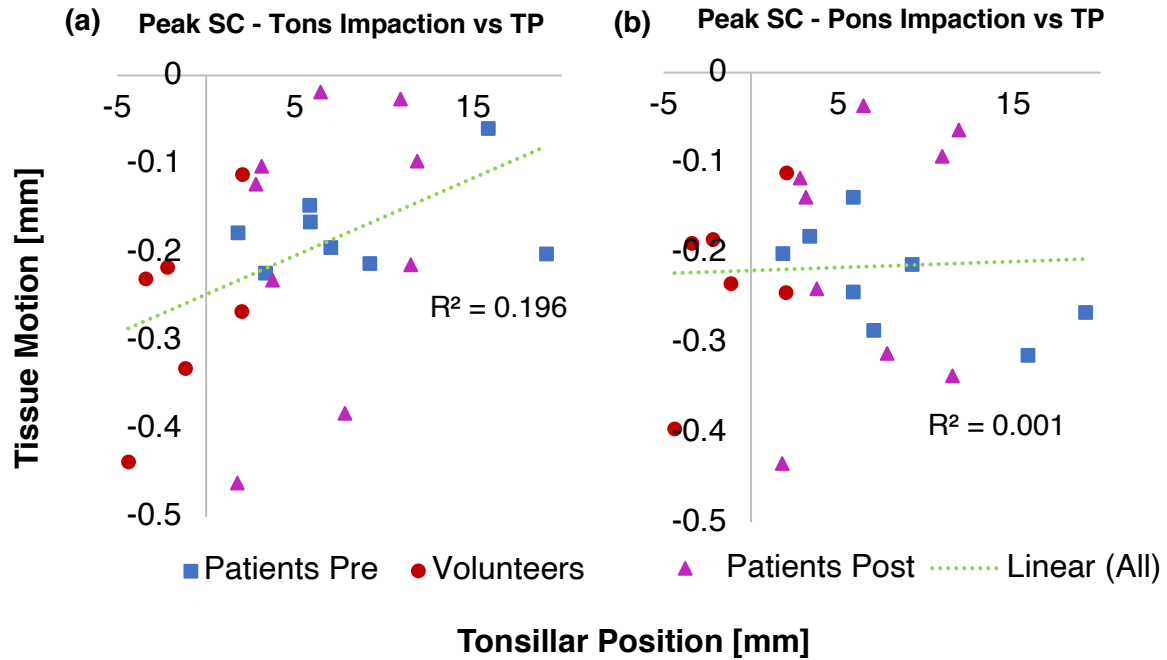


**Figure 4.5.a.** Regression analysis plots for all pre- and post-operative patients and controls showing tonsillar position versus tissue motion for peak impaction of the spinal cord – tons. **b.** Regression analysis plots for all pre- and post-operative patients and controls showing tonsillar position versus tissue motion for peak impaction of the spinal cord – pons.

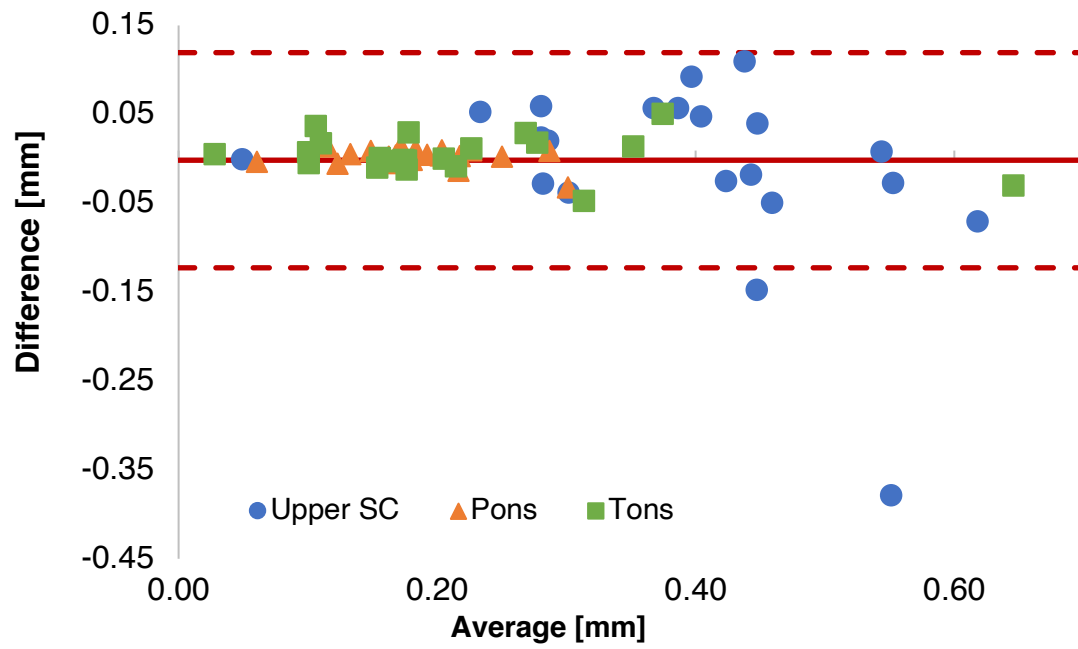


**Figure 4.6.** Bland-Altman of displacement results for each operator.

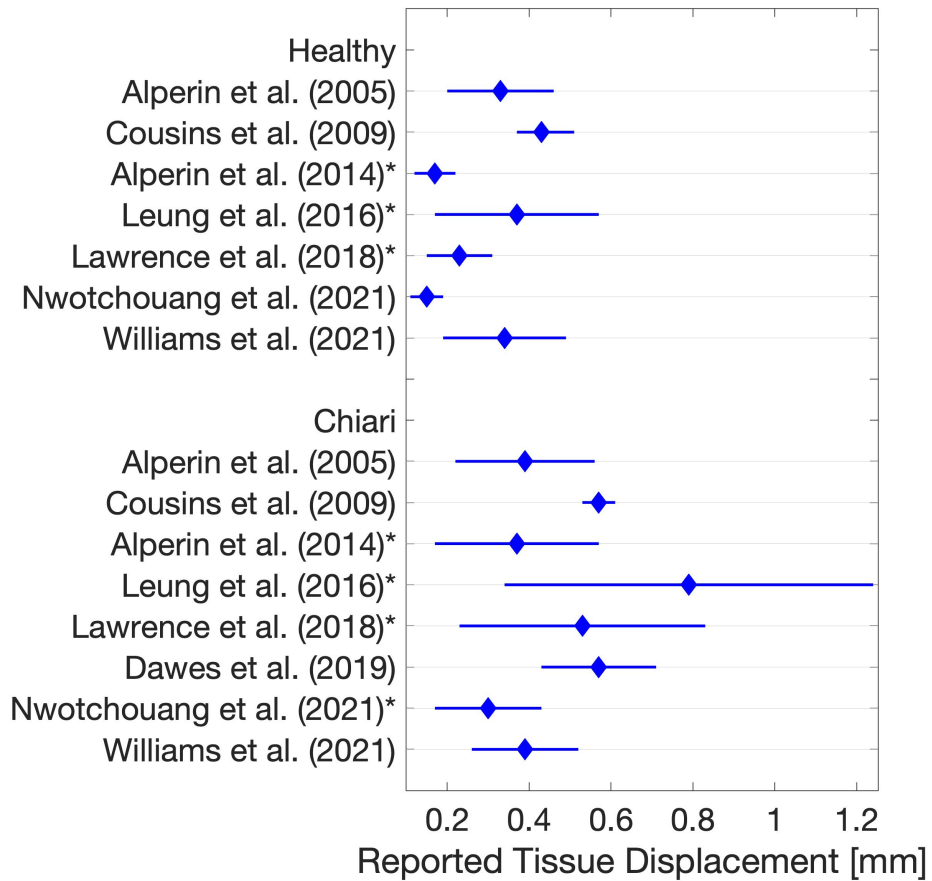


**Figure 4.7.** Forest plot of meta-analysis showing previous studies which reported comparable metrics of tissue motion in the cerebellar tonsils or upper spinal cord. \* represents studies that found a significant difference between pre-operative patients and controls.

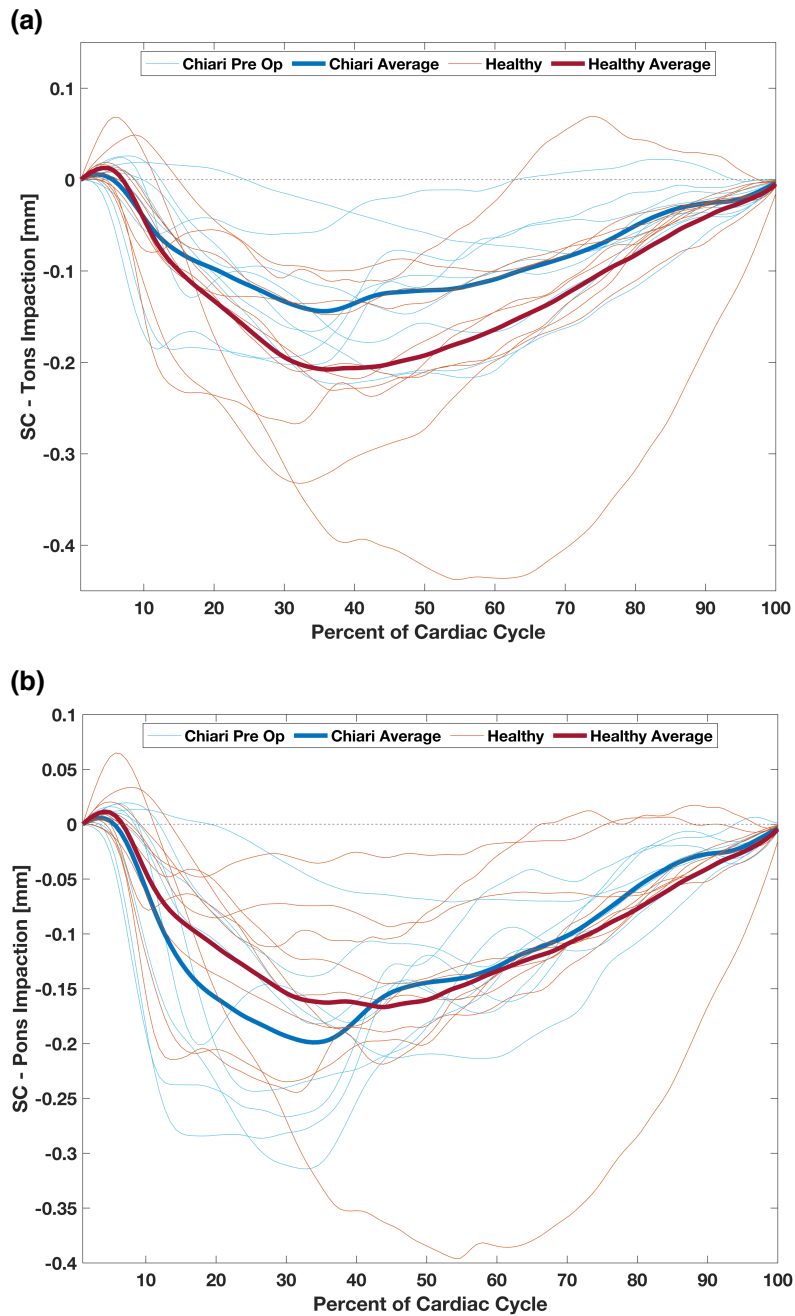


**Figure 4.8.a.** Spinal Cord – tonsil impaction data shown over the cardiac cycle for all pre-operative patients and controls. **b.** Spinal Cord – pons impaction data shown over the cardiac cycle for all pre-operative patients and controls.



## Chapter 5: Conclusion

The need for improved CMI diagnostics results from a lack of understanding of the underlying CMI pathophysiologies that may be an outcome of our lack of accurate and precise imaging methodologies. The barriers to improved CMI diagnostic practices are complex and require solutions that look for an improved understanding of the fundamental CMI pathophysiology while being pragmatic and realistic with outcomes tied directly to clinical application. To satisfactorily address the need for improved CMI diagnostics, a more complete understanding of the underlying CMI pathophysiology must be obtained through development of advanced image analysis and post-processing techniques. First, as discussed in Chapter 3, to address the need for improved image analysis techniques, current standard clinical and research MRI modalities were evaluated for agreement, repeatability, and reproducibility using an in vitro CMI subject specific 3D printed model. We found that PC MRI measurements of CSF at the craniovertebral junction lacked reproducibility between MRI machines, limiting the application of results and comparisons of patient data across scanning centers and varying protocols. Next, as discussed in Chapter 4, to address the need for an improved understanding of the underlying CMI physiology, ten adult CMI patients receiving surgical intervention were compared to ten healthy volunteers pre- and post-operatively using 2D PC MRI to quantify neural tissue motion in healthy and disease states. With more research, relative tissue motion between the spinal cord and neighboring regions could potentially provide a physiological basis for formation of a syrinx and therein provide novel biomarker for improved surgical candidacy selection.

The results presented here could provide a better understanding of PC MRI technique reproducibility and an explanation for the conflicting reports in literature regarding CMI physiologies and CSF characteristics. With more accurate measurement techniques, post-processing techniques such as those used here to quantify CSF velocities and neural tissue motion at the craniovertebral junction will be more directly comparable across literature thereby potentially allowing for an improved functional understanding of the underlying CMI physiology. The combination of improved CMI pathophysiological understanding with advanced imaging and post-processing techniques could benefit the CMI community with improved surgical candidacy selection and a path towards interventions to affect the physiology itself rather than its symptoms.

### Future Directions

While the results presented here could potentially provide a basis for future novel CMI biomarkers, they do not conclusively provide biomarkers at present. Detailed research over larger cohorts should be performed with symptomatic and asymptomatic CMI patients in comparison to each other and controls to investigate relative neural tissue motion at the craniovertebral junction. With improved imaging modalities such as DENSE MRI or 4D Flow, tissue motion of these physiologically regions can be more reliably quantified and understood so that the basis of syrinx formation suggested here may be more conclusively defined. A long-term study following CMI patients with and without symptoms would ideally be performed wherein predications of syrinx formation are made based on relative impaction of the spinal cord compared to the pons and the tonsils. Ideally, spinal cord impaction would provide a basis for surgical candidacy selection so that patients at high risk for syrinx formation may be identified and intervention provided to ensure no syrinx-related nerve damage occurs.

The results here suggest there may be some physiological importance within the relative motion between the spinal cord and neighboring regions in the craniovertebral junction but may not be the ultimate biomarker or predictor for surgical candidacy and syrinx formation risk. The motion defined here is done so in terms of displacement, but this could be taken further to derive tissue strain and tissue strain rates as exerted onto them from the CSF fluid motion. Future studies should be directed towards using advanced imaging techniques with improved temporal-spatial resolution so that craniovertebral tissue motion may be fully characterized in terms of tissue displacement, strain, and strain rate to define a novel biomarker with direct relation to clinical presentation of symptomatology. Notably, the localization of this motion at the cerebellum could affect the mechanical environment of the extracellular matrix (ECM), which has been shown by several studies to affect the mechanical phenotype of cell types that originate from a normal brain, such as astrocytes and neurons [89-91]. With distinct changes to the mechanical environment, it is highly likely that the mechano-signals experienced by cells in the craniovertebral junction are therefore different in the CMI disease state compared to the normal, healthy state. These different mechano-signals cause phenotypical changes to astrocytes and neurons [92], which could result in changes to the functionality of those cells and potentially provide a basis for the varying clinical presentations of CMI. Future studies ought to be performed to fully explore this abnormal physiology in CMI and the effects it has on cellular signaling and functionality to eventually define the relationship between neural tissue strain and higher order brain functions.

Advanced imaging techniques are not strictly required for this research, but instead could be performed with standard 2D PC MRI with improved MRI calibration and optimized dynamic imaging parameters. In combination with advanced post-processing techniques, bulk and relative tissue motion at the craniovertebral junction could be characterized in terms of displacement, strain and strain rate. Use of 2D PC MRI would be specifically advantageous as it would be easily translated into clinical settings as technicians are already familiar with this sequence thereby cutting down training and operational costs associated with novel imaging sequences and additional scan time incurred by less optimized sequences.

## References

1. Speer MC, Enterline DS, Mehlretter L, Hammock P, Joseph J, Dickerson M, Ellenbogen RG, Milhorat TH, Hauser MA, George TM: **Review Article: Chiari Type I Malformation with or Without Syringomyelia: Prevalence and Genetics.** *J Genet Couns* 2003, **12**:297-311.
2. Meadows J, Kraut M, Guarnieri M, Haroun RI, Carson BS: **Asymptomatic Chiari Type I malformations identified on magnetic resonance imaging.** *J Neurosurg* 2000, **92**:920-926.
3. McClugage SG, Oakes WJ: **The Chiari I malformation.** *J Neurosurg Pediatr* 2019, **24**:217-226.
4. Houston JR, Allen NJ, Eppelheimer MS, Bapuraj JR, Biswas D, Allen PA, Vorster SJ, Luciano MG, Loth F: **Evidence for sex differences in morphological abnormalities in type I Chiari malformation.** *Neuroradiol J* 2019, **32**:458-466.
5. Marty P, Urbizu A, Macaya A, Sahuquillo J, Antonia Poca M, Martin B: **Gender-specific differences in adult type I Chiari malformation morphometrics (P4.174).** *Neurology* 2015, **84**:P4.174.
6. Tubbs RS, Beckman J, Naftel RP, Chern JJ, Wellons JC, 3rd, Rozzelle CJ, Blount JP, Oakes WJ: **Institutional experience with 500 cases of surgically treated pediatric Chiari malformation Type I.** *J Neurosurg Pediatr* 2011, **7**:248-256.
7. Humphrey E: **Chiari malformations in adults: their surgical and nursing management.** *British Journal of Neuroscience Nursing* 2019, **15**:130-136.
8. Heiss JD, Argersinger DP: **Epidemiology of Chiari I Malformation.** In *The Chiari Malformations*. Edited by Tubbs RS, Turgut M, Oakes WJ. Cham: Springer International Publishing; 2020: 263-274
9. Vernooij MW, Ikram MA, Tanghe HL, Vincent AJ, Hofman A, Krestin GP, Niessen WJ, Breteler MM, van der Lugt A: **Incidental findings on brain MRI in the general population.** *N Engl J Med* 2007, **357**:1821-1828.
10. O'Reilly EM, Torreggiani W: **Incidence of Asymptomatic Chiari Malformation.** *Ir Med J* 2019, **112**:972.
11. Symms M, Jäger HR, Schmierer K, Yousry TA: **A review of structural magnetic resonance neuroimaging.** *Journal of Neurology, Neurosurgery & Psychiatry* 2004, **75**:1235-1244.
12. Götte MJW, Germans T, Rüssel IK, Zwanenburg JJM, Marcus JT, Rossum ACv, Veldhuisen DJv: **Myocardial Strain and Torsion Quantified by Cardiovascular Magnetic Resonance Tissue Tagging.** *Journal of the American College of Cardiology* 2006, **48**:2002-2011.
13. Adams AL, Kuijff HJ, Viergever MA, Luijten PR, Zwanenburg JJM: **Quantifying cardiac-induced brain tissue expansion using DENSE.** *NMR Biomed* 2019, **32**:e4050.
14. Lindstrom EK, Ringstad G, Mardal KA, Eide PK: **Cerebrospinal fluid volumetric net flow rate and direction in idiopathic normal pressure hydrocephalus.** *Neuroimage Clin* 2018, **20**:731-741.
15. Blitz AM, Shin J, Baledent O, Page G, Bonham LW, Herzka DA, Moghekar AR, Rigamonti D: **Does Phase-Contrast Imaging through the Cerebral Aqueduct Predict the Outcome of Lumbar CSF Drainage or Shunt Surgery in Patients with Suspected Adult Hydrocephalus?** *AJNR Am J Neuroradiol* 2018, **39**:2224-2230.

16. Martin BA, Kalata W, Shaffer N, Fischer P, Luciano M, Loth F: **Hydrodynamic and longitudinal impedance analysis of cerebrospinal fluid dynamics at the craniovertebral junction in type I Chiari malformation.** *PLoS One* 2013, **8**:e75335.
17. Heiss JD, Snyder K, Peterson MM, Patronas NJ, Butman JA, Smith RK, Devroom HL, Sansur CA, Eskioglu E, Kammerer WA, Oldfield EH: **Pathophysiology of primary spinal syringomyelia.** *J Neurosurg Spine* 2012, **17**:367-380.
18. Yeo J, Cheng S, Hemley S, Lee BB, Stoodley M, Bilston L: **Characteristics of CSF Velocity-Time Profile in Posttraumatic Syringomyelia.** *AJNR Am J Neuroradiol* 2017.
19. Shaffer N, Martin B, Loth F: **Cerebrospinal fluid hydrodynamics in type I Chiari malformation.** *Neurol Res* 2011, **33**:247-260.
20. Bapuraj JR, Londy FJ, Delavari N, Maher CO, Garton HJL, Martin BA, Muraszko KM, Ibrahim EH, Quint DJ: **Cerebrospinal fluid velocity amplitudes within the cerebral aqueduct in healthy children and patients with Chiari I malformation.** *Journal of Magnetic Resonance Imaging* 2016, **44**:463-470.
21. Korbecki A, Zimny A, Podgorski P, Sasiadek M, Bladowska J: **Imaging of cerebrospinal fluid flow: fundamentals, techniques, and clinical applications of phase-contrast magnetic resonance imaging.** *Pol J Radiol* 2019, **84**:e240-e250.
22. Krueger KD, Haughton VM, Hetzel S: **Peak CSF velocities in patients with symptomatic and asymptomatic Chiari I malformation.** *AJNR Am J Neuroradiol* 2010, **31**:1837-1841.
23. Geiger J, Markl M, Jung B, Grohmann J, Stiller B, Langer M, Arnold R: **4D-MR flow analysis in patients after repair for tetralogy of Fallot.** *Eur Radiol* 2011, **21**:1651-1657.
24. Barker AJ, Markl M, Burk J, Lorenz R, Bock J, Bauer S, Schulz-Menger J, von Knobelsdorff-Brenkenhoff F: **Bicuspid Aortic Valve Is Associated With Altered Wall Shear Stress in the Ascending Aorta.** *Circulation-Cardiovascular Imaging* 2012, **5**:457-466.
25. Stadlbauer A, Salomonowitz E, van der Riet W, Buchfelder M, Ganslandt O: **Insight into the patterns of cerebrospinal fluid flow in the human ventricular system using MR velocity mapping.** *Neuroimage* 2010, **51**:42-52.
26. Stankovic Z, Allen BD, Garcia J, Jarvis KB, Markl M: **4D flow imaging with MRI.** *Cardiovasc Diagn Ther* 2014, **4**:173-192.
27. Bunck AC, Kroeger JR, Juettner A, Brentrup A, Fiedler B, Crelier GR, Martin BA, Heindel W, Maintz D, Schwindt W, Niederstadt T: **Magnetic resonance 4D flow analysis of cerebrospinal fluid dynamics in Chiari I malformation with and without syringomyelia.** *European Radiology* 2012, **22**:1860-1870.
28. Watts R, Steinklein JM, Waldman L, Zhou X, Filippi CG: **Measuring Glymphatic Flow in Man Using Quantitative Contrast-Enhanced MRI.** *AJNR Am J Neuroradiol* 2019, **40**:648-651.
29. Edeklev CS, Halvorsen M, Lovland G, Vatnehol SAS, Gjertsen O, Nedregard B, Sletteberg R, Ringstad G, Eide PK: **Intrathecal Use of Gadobutrol for Glymphatic MR Imaging: Prospective Safety Study of 100 Patients.** *AJNR Am J Neuroradiol* 2019, **40**:1257-1264.
30. Eide PK, Ringstad G: **Delayed clearance of cerebrospinal fluid tracer from entorhinal cortex in idiopathic normal pressure hydrocephalus: A glymphatic magnetic resonance imaging study.** *J Cereb Blood Flow Metab* 2019, **39**:1355-1368.
31. Yildiz S, Thyagaraj S, Jin N, Zhong X, Heidari Pahlavian S, Martin BA, Loth F, Oshinski J, Sabra KG: **Quantifying the influence of respiration and cardiac pulsations on**

- cerebrospinal fluid dynamics using real-time phase-contrast MRI. *J Magn Reson Imaging* 2017, **46**:431-439.
32. Chen L, Beckett A, Verma A, Feinberg DA: **Dynamics of respiratory and cardiac CSF motion revealed with real-time simultaneous multi-slice EPI velocity phase contrast imaging.** *Neuroimage* 2015, **122**:281-287.
  33. Aktas G, Kollmeier JM, Joseph AA, Merboldt KD, Ludwig HC, Gartner J, Frahm J, Dreha-Kulaczewski S: **Spinal CSF flow in response to forced thoracic and abdominal respiration.** *Fluids Barriers CNS* 2019, **16**:10.
  34. Dreha-Kulaczewski S, Konopka M, Joseph AA, Kollmeier J, Merboldt KD, Ludwig HC, Gartner J, Frahm J: **Respiration and the watershed of spinal CSF flow in humans.** *Sci Rep* 2018, **8**:5594.
  35. Yamada S, Miyazaki M, Yamashita Y, Ouyang C, Yui M, Nakahashi M, Shimizu S, Aoki I, Morohoshi Y, McComb JG: **Influence of respiration on cerebrospinal fluid movement using magnetic resonance spin labeling.** *Fluids Barriers CNS* 2013, **10**:36.
  36. Yamada S, Goto T: **[Understanding of cerebrospinal fluid hydrodynamics in idiopathic hydrocephalus (A) Visualization of CSF bulk flow with MRI time-spatial labeling pulse method (time-SLIP)].** *Rinsho Shinkeigaku* 2010, **50**:966-970.
  37. Luciano MG, Batzdorf U, Kula RW, Rocque BG, Maher CO, Heiss J, Martin BA, Bolognese PA, Ashley-Koch A, Limbrick D, et al: **Development of Common Data Elements for Use in Chiari Malformation Type I Clinical Research: An NIH/NINDS Project.** *Neurosurgery* 2019, **85**:854-860.
  38. Haughton VM, Korosec FR, Medow JE, Dolar MT, Iskandar BJ: **Peak systolic and diastolic CSF velocity in the foramen magnum in adult patients with Chiari I malformations and in normal control participants.** *American Journal of Neuroradiology* 2003, **24**:169-176.
  39. Quigley MF, Iskandar B, Quigley ME, Nicosia M, Haughton V: **Cerebrospinal fluid flow in foramen magnum: Temporal and spatial patterns at MR imaging in volunteers and in patients with Chiari I malformation.** *Radiology* 2004, **232**:229-236.
  40. McGirt MJ, Atiba A, Attenello FJ, Wasserman BA, Datto G, Gathinji M, Carson B, Weingart JD, Jallo GI: **Correlation of hindbrain CSF flow and outcome after surgical decompression for Chiari I malformation.** *Childs Nerv Syst* 2008, **24**:833-840.
  41. Sakas DE, Korfiatis SI, Wayte SC, Beale DJ, Papapetrou KP, Stranjalis GS, Whittaker KW, Whitwell HL: **Chiari malformation: CSF flow dynamics in the craniocervical junction and syrinx.** *Acta Neurochir (Wien)* 2005, **147**:1223-1233.
  42. Thyagaraj S, Pahlavian SH, Sass LR, Loth F, Vatani M, Choi JW, Tubbs RS, Giese D, Kroger JR, Bunck AC, Martin BA: **An MRI-Compatible Hydrodynamic Simulator of Cerebrospinal Fluid Motion in the Cervical Spine.** *IEEE Trans Biomed Eng* 2017.
  43. Wentland AL, Grist TM, Wieben O: **Repeatability and internal consistency of abdominal 2D and 4D phase contrast MR flow measurements.** *Acad Radiol* 2013, **20**:699-704.
  44. Frydrychowicz A, Wieben O, Niespodzany E, Reeder SB, Johnson KM, Francois CJ: **Quantification of thoracic blood flow using volumetric magnetic resonance imaging with radial velocity encoding: in vivo validation.** *Invest Radiol* 2013, **48**:819-825.
  45. Drangova M, Zhu Y, Pelc NJ: **Effect of artifacts due to flowing blood on the reproducibility of phase-contrast measurements of myocardial motion.** *J Magn Reson Imaging* 1997, **7**:664-668.
  46. Sakhare AR, Barisano G, Pa J: **Assessing test-retest reliability of phase contrast MRI for measuring cerebrospinal fluid and cerebral blood flow dynamics.** *Magn Reson Med* 2019, **82**:658-670.

47. Heidari Pahlavian S, Bunck AC, Thyagaraj S, Giese D, Loth F, Hedderich DM, Kroger JR, Martin BA: **Accuracy of 4D Flow Measurement of Cerebrospinal Fluid Dynamics in the Cervical Spine: An In Vitro Verification Against Numerical Simulation.** *Ann Biomed Eng* 2016, **44**:3202-3214.
48. Meckel S, Leitner L, Bonati LH, Santini F, Schubert T, Stalder AF, Lyrer P, Markl M, Wetzel SG: **Intracranial artery velocity measurement using 4D PC MRI at 3 T: comparison with transcranial ultrasound techniques and 2D PC MRI.** *Neuroradiology* 2013, **55**:389-398.
49. Feneis JF, Kyubwa E, Atianzar K, Cheng JY, Alley MT, Vasanaawala SS, Demaria AN, Hsiao A: **4D flow MRI quantification of mitral and tricuspid regurgitation: Reproducibility and consistency relative to conventional MRI.** *J Magn Reson Imaging* 2018, **48**:1147-1158.
50. Stalder AF, Russe MF, Frydrychowicz A, Bock J, Hennig J, Markl M: **Quantitative 2D and 3D phase contrast MRI: optimized analysis of blood flow and vessel wall parameters.** *Magn Reson Med* 2008, **60**:1218-1231.
51. Gabbour M, Schnell S, Jarvis K, Robinson JD, Markl M, Rigsby CK: **4-D flow magnetic resonance imaging: blood flow quantification compared to 2-D phase-contrast magnetic resonance imaging and Doppler echocardiography.** *Pediatr Radiol* 2015, **45**:804-813.
52. Yzet T, Bouzerar R, Allart JD, Demuynck F, Legallais C, Robert B, Deramond H, Meyer ME, Baledent O: **Hepatic vascular flow measurements by phase contrast MRI and doppler echography: a comparative and reproducibility study.** *J Magn Reson Imaging* 2010, **31**:579-588.
53. Alperin N, Hushek SG, Lee SH, Sivaramakrishnan A, Lichtor T: **MRI study of cerebral blood flow and CSF flow dynamics in an upright posture: the effect of posture on the intracranial compliance and pressure.** *Acta Neurochir Suppl* 2005, **95**:177-181.
54. Alperin N, Loftus JR, Olius CJ, Bagci AM, Lee SH, Ertl-Wagner B, Green B, Sekula R: **Magnetic resonance imaging measures of posterior cranial fossa morphology and cerebrospinal fluid physiology in Chiari malformation type I.** *Neurosurgery* 2014, **75**:515-522; discussion 522.
55. Alperin N, Lee SH, Bagci AM: **MRI measurements of intracranial pressure in the upright posture: The effect of the hydrostatic pressure gradient.** *J Magn Reson Imaging* 2015, **42**:1158-1163.
56. Tawfik AM, Elsorogy L, Abdelghaffar R, Naby AA, Elmenshawi I: **Phase-Contrast MRI CSF Flow Measurements for the Diagnosis of Normal-Pressure Hydrocephalus: Observer Agreement of Velocity Versus Volume Parameters.** *AJR Am J Roentgenol* 2017, **208**:838-843.
57. Luetmer PH, Huston J, Friedman JA, Dixon GR, Petersen RC, Jack CR, McClelland RL, Ebersold MJ: **Measurement of cerebrospinal fluid flow at the cerebral aqueduct by use of phase-contrast magnetic resonance imaging: technique validation and utility in diagnosing idiopathic normal pressure hydrocephalus.** *Neurosurgery* 2002, **50**:534-543; discussion 543-534.
58. Martin BA, Yiallourou TI, Pahlavian SH, Thyagaraj S, Bunck AC, Loth F, Sheffer DB, Kroger JR, Stergiopoulos N: **Inter-operator Reliability of Magnetic Resonance Image-Based Computational Fluid Dynamics Prediction of Cerebrospinal Fluid Motion in the Cervical Spine.** *Ann Biomed Eng* 2016, **44**:1524-1537.
59. Yamada S, Tsuchiya K, Bradley WG, Law M, Winkler ML, Borzage MT, Miyazaki M, Kelly EJ, McComb JG: **Current and emerging MR imaging techniques for the**

- diagnosis and management of CSF flow disorders: a review of phase-contrast and time-spatial labeling inversion pulse.** *AJNR Am J Neuroradiol* 2015, **36**:623-630.
60. Yiallourou TI, Kroger JR, Stergiopoulos N, Maintz D, Martin BA, Bunck AC: **Comparison of 4D phase-contrast MRI flow measurements to computational fluid dynamics simulations of cerebrospinal fluid motion in the cervical spine.** *PLoS One* 2012, **7**:e52284.
61. Yamada S: **Cerebrospinal fluid physiology: visualization of cerebrospinal fluid dynamics using the magnetic resonance imaging Time-Spatial Inversion Pulse method.** *Croat Med J* 2014, **55**:337-346.
62. Heidari Pahlavian S, Bunck AC, Loth F, Shane Tubbs R, Yiallourou T, Kroeger JR, Heindel W, Martin BA: **Characterization of the discrepancies between four-dimensional phase-contrast magnetic resonance imaging and in-silico simulations of cerebrospinal fluid dynamics.** *J Biomech Eng* 2015, **137**:051002.
63. Peters K, Weiss K, Maintz D, Giese D: **Influence of respiration-induced B0 variations in real-time phase-contrast echo planar imaging of the cervical cerebrospinal fluid.** *Magn Reson Med* 2019, **82**:647-657.
64. Thyagaraj S, Pahlavian SH, Sass LR, Loth F, Vatani M, Choi JW, Tubbs RS, Giese D, Kroger JR, Bunck AC, Martin BA: **An MRI-Compatible Hydrodynamic Simulator of Cerebrospinal Fluid Motion in the Cervical Spine.** *IEEE Trans Biomed Eng* 2018, **65**:1516-1523.
65. Walker PG, Cranney GB, Scheidegger MB, Waseleski G, Pohost GM, Yoganathan AP: **Semiautomated method for noise reduction and background phase error correction in MR phase velocity data.** *J Magn Reson Imaging* 1993, **3**:521-530.
66. Glor FP, Long Q, Hughes AD, Augst AD, Ariff B, Thom SA, Verdonck PR, Xu XY: **Reproducibility study of magnetic resonance image-based computational fluid dynamics prediction of carotid bifurcation flow.** *Ann Biomed Eng* 2003, **31**:142-151.
67. Bunck AC, Kroger JR, Juttner A, Brentrup A, Fiedler B, Schaarschmidt F, Crelier GR, Schwindt W, Heindel W, Niederstadt T, Maintz D: **Magnetic resonance 4D flow characteristics of cerebrospinal fluid at the craniocervical junction and the cervical spinal canal.** *Eur Radiol* 2011, **21**:1788-1796.
68. Yiallourou TI, Kröger JR, Stergiopoulos N, Maintz D, Martin BA, Bunck AC: **Comparison of 4D Phase-Contrast MRI Flow Measurements to Computational Fluid Dynamics Simulations of Cerebrospinal Fluid Motion in the Cervical Spine.** *PLoS ONE* 2012, **7**:e52284.
69. Shah S, Haughton V, del Rio AM: **CSF flow through the upper cervical spinal canal in Chiari I malformation.** *AJNR Am J Neuroradiol* 2011, **32**:1149-1153.
70. Haughton VM, Korosec FR, Medow JE, Dolar MT, Iskandar BJ: **Peak systolic and diastolic CSF velocity in the foramen magnum in adult patients with Chiari I malformations and in normal control participants.** *AJNR Am J Neuroradiol* 2003, **24**:169-176.
71. Dolar MT, Haughton VM, Iskandar BJ, Quigley M: **Effect of craniocervical decompression on peak CSF velocities in symptomatic patients with Chiari I malformation.** *AJNR Am J Neuroradiol* 2004, **25**:142-145.
72. Hofmann E, Warmuth-Metz M, Bendszus M, Solymosi L: **Phase-contrast MR imaging of the cervical CSF and spinal cord: volumetric motion analysis in patients with Chiari I malformation.** *AJNR Am J Neuroradiol* 2000, **21**:151-158.
73. Iskandar BJ, Quigley M, Haughton VM: **Foramen magnum cerebrospinal fluid flow characteristics in children with Chiari I malformation before and after craniocervical decompression.** *J Neurosurg* 2004, **101**:169-178.



74. Rutkowska G, Haughton V, Linge S, Mardal KA: **Patient-specific 3D simulation of cyclic CSF flow at the craniocervical region.** *AJNR Am J Neuroradiol* 2012, **33**:1756-1762.
75. Loth F, Yardimci MA, Alperin N: **Hydrodynamic modeling of cerebrospinal fluid motion within the spinal cavity.** *J Biomech Eng* 2001, **123**:71-79.
76. Cheng S, Stoodley MA, Wong J, Hemley S, Fletcher DF, Bilston LE: **The presence of arachnoiditis affects the characteristics of CSF flow in the spinal subarachnoid space: a modelling study.** *J Biomech* 2012, **45**:1186-1191.
77. Alperin N, Loftus JR, Bagci AM, Lee SH, Oliu CJ, Green BA: **Magnetic resonance imaging-based measures predictive of short-term surgical outcome in patients with Chiari malformation Type I.** *Journal of Neurology, Neurosurgery, and Psychiatry* 2015.
78. Koerte I, Haberl C, Schmidt M, Pomschar A, Lee S, Rapp P, Steffinger D, Tain RW, Alperin N, Ertl-Wagner B: **Inter- and intra-rater reliability of blood and cerebrospinal fluid flow quantification by phase-contrast MRI.** *J Magn Reson Imaging* 2013, **38**:655-662.
79. Holly LT, Batzdorf U: **Chiari malformation and syringomyelia.** *J Neurosurg Spine* 2019, **31**:619-628.
80. Gomez AD, Knutsen AK, Xing F, Lu YC, Chan D, Pham DL, Bayly P, Prince JL: **3-D Measurements of Acceleration-Induced Brain Deformation via Harmonic Phase Analysis and Finite-Element Models.** *IEEE Trans Biomed Eng* 2019, **66**:1456-1467.
81. Nwotchouang BST, Eppelheimer MS, Pahlavian SH, Barrow JW, Barrow DL, Qiu D, Allen PA, Oshinski JN, Amini R, Loth F: **Regional Brain Tissue Displacement and Strain is Elevated in Subjects with Chiari Malformation Type I Compared to Healthy Controls: A Study Using DENSE MRI.** *Ann Biomed Eng* 2021.
82. Soellinger M, Rutz AK, Kozerke S, Boesiger P: **3D cine displacement-encoded MRI of pulsatile brain motion.** *Magn Reson Med* 2009, **61**:153-162.
83. Lawrence BJ, Luciano M, Tew J, Ellenbogen RG, Oshinski JN, Loth F, Culley AP, Martin BA: **Cardiac-Related Spinal Cord Tissue Motion at the Foramen Magnum is Increased in Patients with Type I Chiari Malformation and Decreases Postdecompression Surgery.** *World Neurosurg* 2018, **116**:e298-e307.
84. Terae S, Miyasaka K, Abe S, Abe H, Tashiro K: **Increased pulsatile movement of the hindbrain in syringomyelia associated with the Chiari malformation: cine-MRI with presaturation bolus tracking.** *Neuroradiology* 1994, **36**:125-129.
85. Pujol J, Roig C, Capdevila A, Pou A, Marti-Vilalta JL, Kulisevsky J, Escartin A, Zannoli G: **Motion of the cerebellar tonsils in Chiari type I malformation studied by cine phase-contrast MRI.** *Neurology* 1995, **45**:1746-1753.
86. Leung V, Magnussen JS, Stoodley MA, Bilston LE: **Cerebellar and hindbrain motion in Chiari malformation with and without syringomyelia.** *J Neurosurg Spine* 2016, **24**:546-555.
87. Cousins J, Haughton V: **Motion of the cerebellar tonsils in the foramen magnum during the cardiac cycle.** *AJNR Am J Neuroradiol* 2009, **30**:1587-1588.
88. Arava Y, Wang Y, Storey JD, Liu CL, Brown PO, Herschlag D: **Genome-wide analysis of mRNA translation profiles in *Saccharomyces cerevisiae*.** *Proc Natl Acad Sci U S A* 2003, **100**:3889-3894.
89. Georges PC, Miller WJ, Meaney DF, Sawyer ES, Janmey PA: **Matrices with compliance comparable to that of brain tissue select neuronal over glial growth in mixed cortical cultures.** *Biophys J* 2006, **90**:3012-3018.

90. Seidlits SK, Khaing ZZ, Petersen RR, Nickels JD, Vanscoy JE, Shear JB, Schmidt CE: **The effects of hyaluronic acid hydrogels with tunable mechanical properties on neural progenitor cell differentiation.** *Biomaterials* 2010, **31**:3930-3940.
91. Keung AJ, de Juan-Pardo EM, Schaffer DV, Kumar S: **Rho GTPases mediate the mechanosensitive lineage commitment of neural stem cells.** *Stem Cells* 2011, **29**:1886-1897.
92. Pogoda K, Janmey PA: **Glial Tissue Mechanics and Mechanosensing by Glial Cells.** *Front Cell Neurosci* 2018, **12**:25.

## Appendix A

### Tables

**Table A.1.** Effect sizes and corresponding p values estimated from the secondary linear mixed-effects model for velocity measurements. This model uses Center 2 as the baseline and includes interactions between scanning modality, scanning center, and axial position of imaging. The mean effect size is provided, along with the 95% confidence interval (CI). We used Bonferroni correction to account for multiple testing. \* represents statistical significance under Bonferroni correction where the threshold is  $p < 0.05/14=0.0036$ .

Effect	Effect Size (95% CI) [cm/s]	p value
Intercept (Center 2: 2D PC MRI at FM)	13.70 (13.27, 14.14)	$4.57 \times 10^{-14}$ *
Scan type (4D – 2D)	-0.02 (-0.28, 0.24)	0.86
Center 1	0.45 (-0.36, 1.27)	0.27
Center 3	-1.64 (-2.29, -0.99)	0.11
Center 4	-2.06 (-2.44, -1.69)	$1.40 \times 10^{-06}$ *
Center 5	-0.72 (-1.59, 0.15)	$4.17 \times 10^{-22}$ *
C1	-0.80 (-1.36, -0.24)	0.01
C2M	-0.49 (-0.96, -0.02)	0.04
C2B	0.01 (-0.45, 0.48)	0.95
C3	-1.21 (-1.67, -0.75)	$5.78 \times 10^{-07}$ *
C4	-1.36 (-1.85, -0.87)	$1.01 \times 10^{-07}$ *
C5	-0.54 (-1.14, 0.07)	0.08
C6	-1.26 (-1.77, -0.75)	$1.89 \times 10^{-06}$ *
C7	-1.71 (-2.17, -1.24)	$8.37 \times 10^{-12}$ *

## Figures

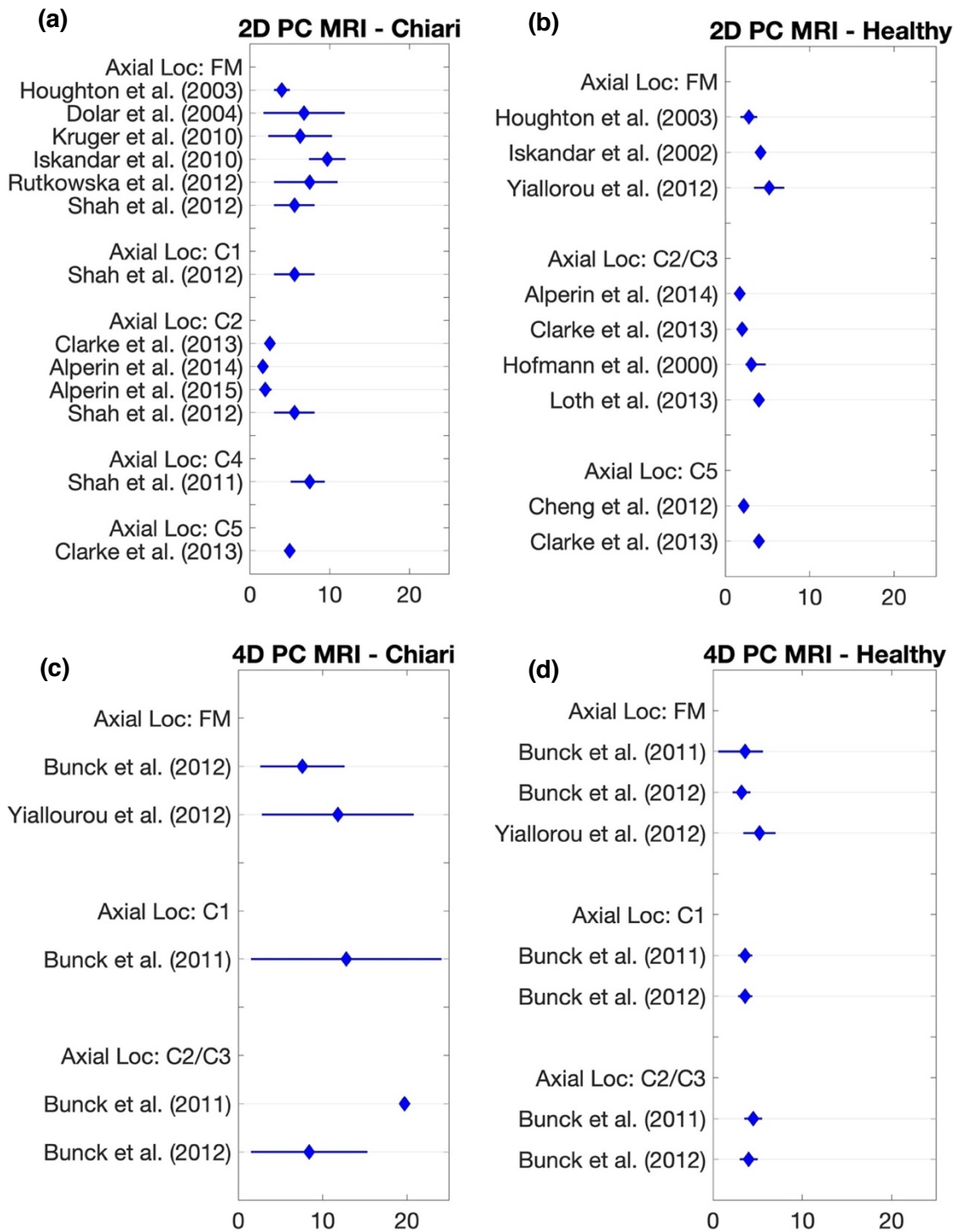


**Figure A.1.** Forest Plot of meta-analysis separated by imaging modality (2D PC MRI and 4D PC MRI) and Chiari vs healthy populations. **(a)** 2D PC MRI reported results for Chiari subjects. **(b)** 2D PC MRI reported results for healthy volunteers. **(c)** 4D PC MRI reported results for Chiari subjects. **(d)** 4D PC MRI reported results for healthy volunteers.

## Appendix B

### Tables

**Table B.1.** Pearson correlation coefficients (CC) for peak spinal cord impaction and tonsillar position for each group.

		<b>CC</b>
<b>Pre</b>	Peak SC-Tonsil	0.33
	Peak SC-Pons	-0.64
<b>Control</b>	Peak SC-Tonsil	0.61
	Peak SC-Pons	0.57
<b>Post</b>	Peak SC-Tonsil	0.34
	Peak SC-Pons	0.24

## Figures

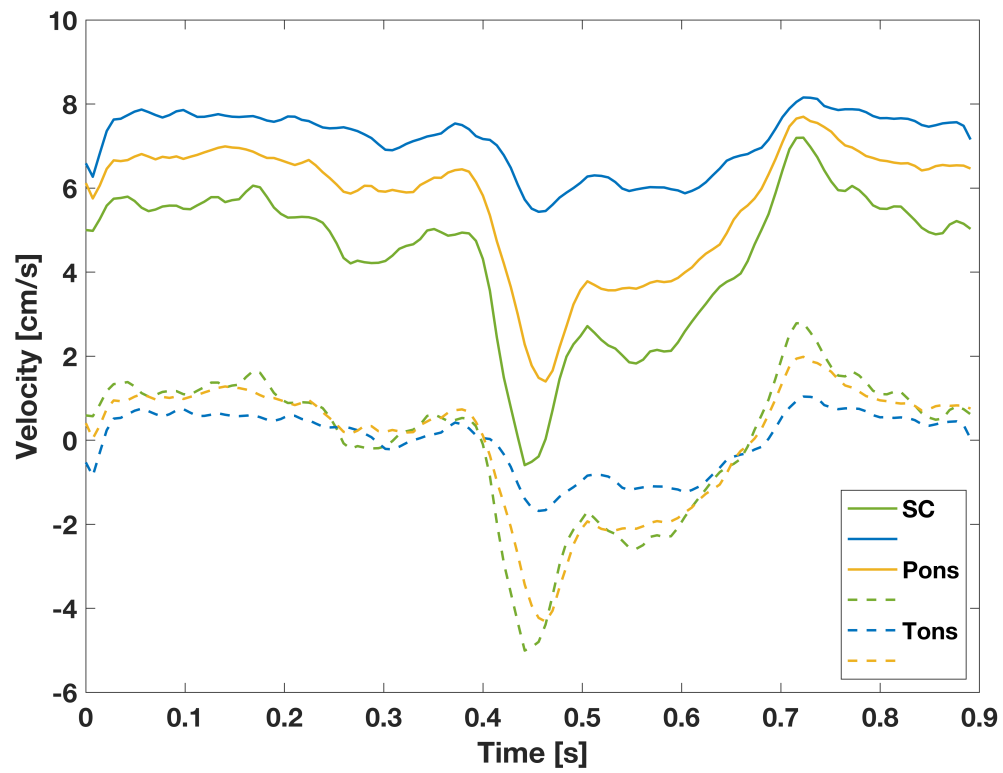


**Figure B.1.** Velocity timeseries data for representative subject p04 before and after applying net-zero velocity constraint.

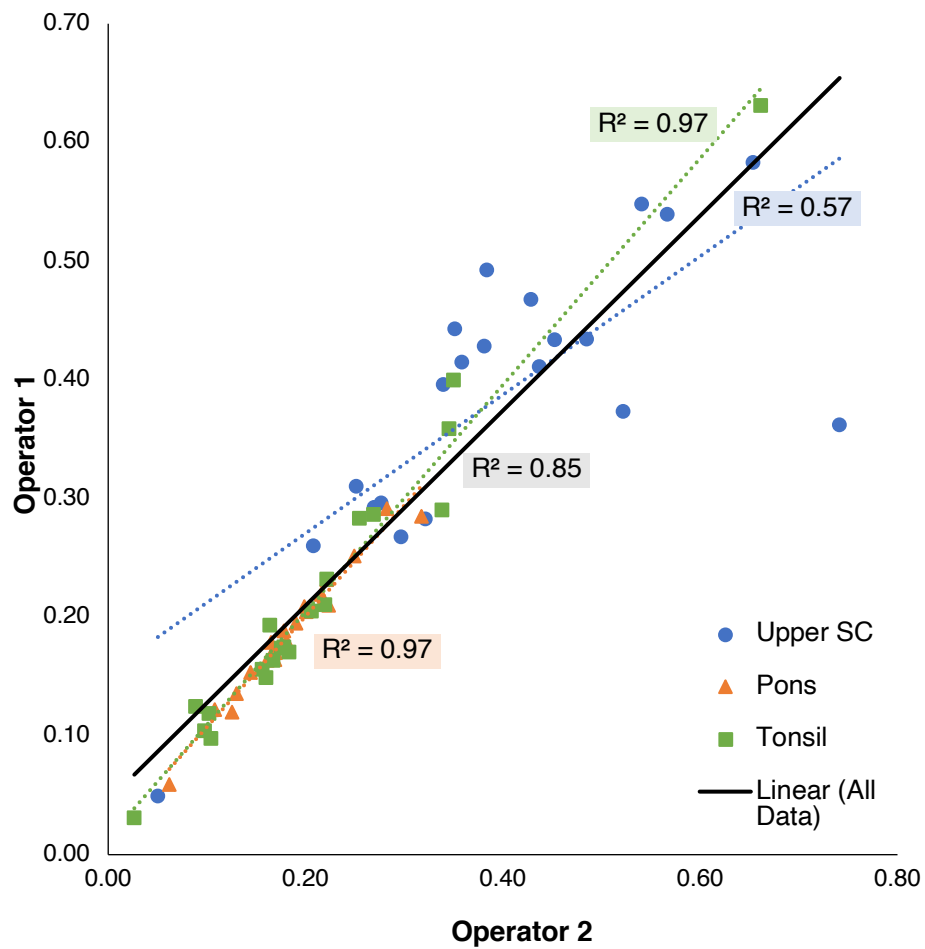


**Figure B.2.** Regression analysis of operators 1 and 2 with linear trendlines shown for each region and  $R^2$  reported with color coding for respective regions of interest (ROIs): upper SC = spinal cord, pons, and tonsil. Black line represents linear trendline for all data points, with  $R^2$  shaded with grey.

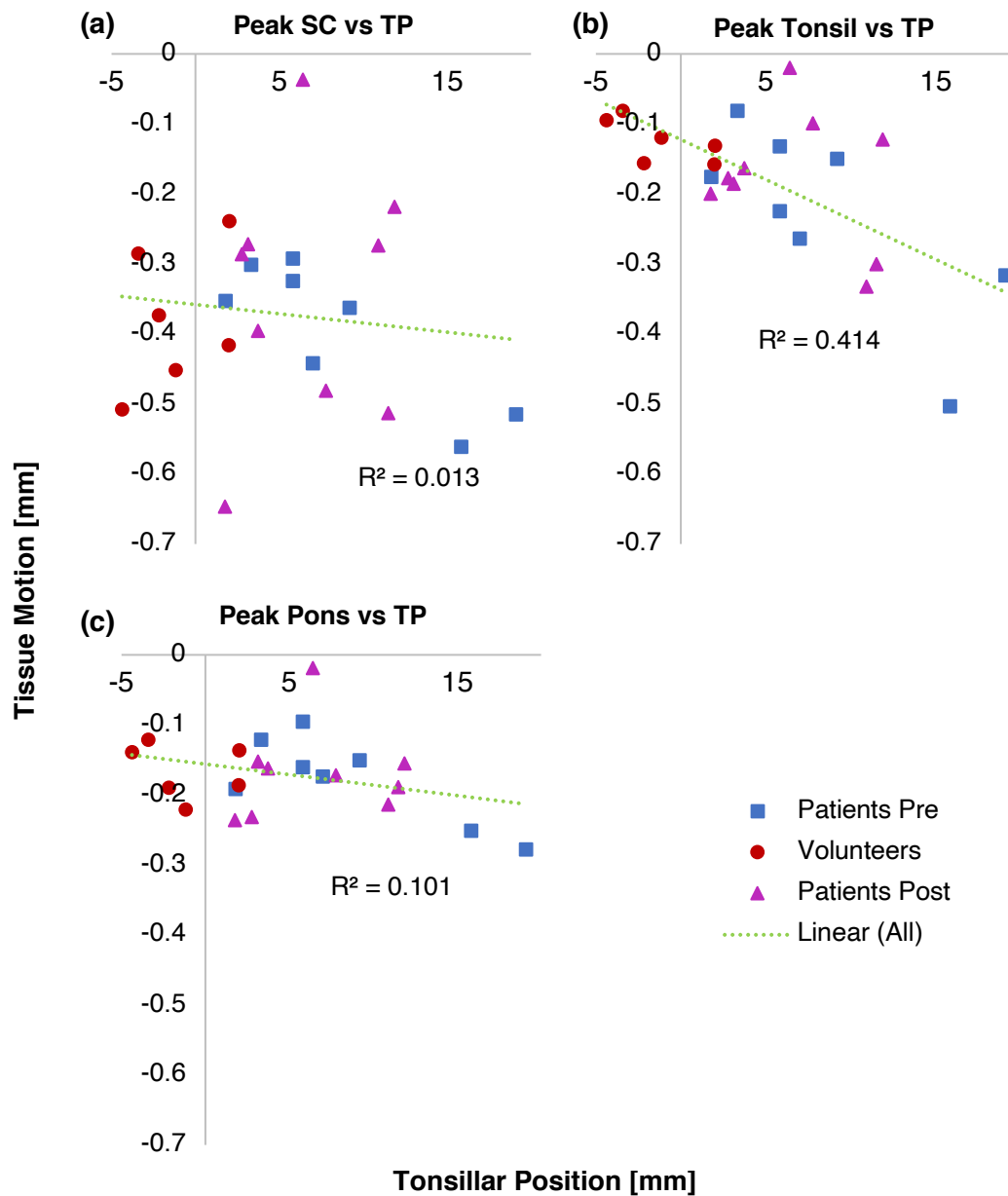


**Figure B.3.** Regression analysis plots for tonsillar position (TP) measurements vs each region of interest (ROI) investigated here (spinal cord = SC, tonsil, pons) for all patients and controls. Green dotted lines represent linear trendline of the data with  $R^2$  reported. (a) Peak absolute spinal cord motion versus tonsillar position. (b) Peak absolute cerebellar tonsil motion versus tonsillar position. (c) Peak absolute pons motion versus tonsillar position.



## Appendix C: Institutional Review Board Approval Letter

9/14/2016

<https://eresearch.emory.edu/Emory/Doc/0/HPO9Q0N9NTMK961CQUMJ6EG486/fromString.html>


EMORY  
UNIVERSITY

Institutional Review Board

TO: John Oshinski, PhD  
Principal Investigator  
\*SOM: Rad: Admin

DATE: April 6, 2016

RE: **Continuing Review Expedited Approval**  
CR6\_IRB00008711

IRB00008711  
Clinical Utility of MRI based Hydrodynamic Parameters in Chiari Malformation

Thank you for submitting a renewal application for this protocol. The Emory IRB reviewed it by the expedited process on 4/5/2016, per 45 CFR 46.110, the Federal Register expedited review categories F4 and F5, and/or 21 CFR 56.110. This reapproval is effective from **4/5/2016** through **4/4/2017**. Thereafter, continuation of human subjects research activities requires the submission of another renewal application, which must be reviewed and approved by the IRB prior to the expiration date noted above. The following consent and authorization documents are approved for use in the new approval period:

- Consent form, version date 6/24/2010
- HIPAA authorization form, version date 4/26/2010
- Revocation letter, version date 3/10/2010

Any reportable events (e.g., unanticipated problems involving risk to subjects or others, noncompliance, breaches of confidentiality, HIPAA violations, protocol deviations) must be reported to the IRB according to our Policies & Procedures at [www.irb.emory.edu](http://www.irb.emory.edu), immediately, promptly, or periodically. Be sure to check the reporting guidance and contact us if you have questions. Terms and conditions of sponsors, if any, also apply to reporting.

Before implementing any change to this protocol (including but not limited to sample size, informed consent, and study design), you must submit an amendment request and secure IRB approval.

In future correspondence about this matter, please refer to the IRB file ID, name of the Principal Investigator, and study title. Thank you.

Sincerely,

Sam Roberts, CIP  
Research Protocol Analyst, Sr.  
*This letter has been digitally signed*

CC: Emory Jessica SOM: Neurology: Neuromuscular  
Sarda Samir \*SOM: Rad Onc: Admin

<https://eresearch.emory.edu/Emory/Doc/0/HPO9Q0N9NTMK961CQUMJ6EG486/fromString.html>

1/2

9/14/2016

<https://eresearch.emory.edu/Emory/Doc/0/HPO9Q0N9NTMK961CQUMJ6EG486/fromString.html>

Barrow	Daniel	*SOM: Neurosurgery: Admin
Holder	Chad	*SOM: Rad: Admin
Saindane	Amit	*SOM: Rad: Admin

---

Emory University  
1599 Clifton Road, 5th Floor - Atlanta, Georgia 30322  
Tel: 404.712.0720 - Fax: 404.727.1358 - Email: [irb@emory.edu](mailto:irb@emory.edu) - Web: <http://www.irb.emory.edu/>  
*An equal opportunity, affirmative action university*